

# The Near-Infrared Spectrum of the Nuclear Star Cluster: Looking Below the Tip of the Iceberg and Comparisons with Extragalactic Nuclei

T. J. Davidge

*Dominion Astrophysical Observatory,  
Herzberg Astronomy & Astrophysics Research Center,  
National Research Council of Canada, 5071 West Saanich Road,  
Victoria, BC Canada V9E 2E7  
tim.davidge@nrc.ca; tdavidge1450@gmail.com*

## ABSTRACT

Long-slit near-infrared (NIR) spectra of the Galactic nuclear star cluster (NSC) are discussed. The spectra sample the major axis of the NSC out to its half light radius. The absorption spectrum of the central regions of the NSC is averaged over angular scales of tens of arc seconds in order to sample globular cluster-like total luminosities, and the results are compared with model spectra. The equivalent widths of NaI2.21 $\mu$ m and CaI2.26 $\mu$ m outside of the center of the NSC, where light from nuclear bulge stars contributes a large fraction to the total flux, are consistent with solar chemical mixtures. In contrast, the equivalent widths of NaI2.21 $\mu$ m and CaI2.26 $\mu$ m near the center of the NSC are larger than expected from models with solar chemical mixtures, even after light from the brightest evolved stars is removed. The depths of spectroscopic features changing along the major axis of the NSC is consistent with imaging studies that have found evidence of population gradients in the NSC. That NaI2.21 $\mu$ m and CaI2.26 $\mu$ m are deeper than predicted for solar chemical mixtures over a range of evolutionary states is consistent with previous studies that find that the majority of stars near the center of the NSC formed from material that had non-solar chemical mixtures. The depths of the NaI2.21 $\mu$ m and CaI2.26 $\mu$ m features in the central regions of the NSC are comparable to those in the nuclear spectrum of

---

<sup>1</sup>Based on observations obtained at the Gemini Observatory, which is operated by the Association of Universities for Research in Astronomy, Inc., under a cooperative agreement with the NSF on behalf of the Gemini partnership: the National Science Foundation (United States), the National Research Council (Canada), CONICYT (Chile), Ministério da Ciência, Tecnologia e Inovação (Brazil) and Ministerio de Ciencia, Tecnología e Innovación Productiva (Argentina).

the early-type Virgo disk galaxy NGC 4491, and are deeper than in the central spectra of NGC 253 and 7793. A spectrum of nebular emission and the youngest stars near the GC is also extracted. The equivalent widths of emission features in the extracted NIR spectrum are similar to those in the nuclear spectrum of NGC 253, and it is argued that this agreement is best achieved if the current episode of star formation near the center of the NSC has been in progress for at least a few Myr.

## 1. INTRODUCTION

The Galactic center (GC) is a unique laboratory for examining the environment near a super-massive black hole (SMBH). With the development of speckle imaging and adaptive optics (AO) systems on large telescopes it has become possible to resolve individual stars within the central parsec of the Galaxy, enabling studies of their spectral energy distribution (SEDs; e.g. Eisenhauer et al. 2005; Buchholz et al. 2009) and motions (e.g. Eckart & Genzel 1997; Ghez et al. 1998; Gillessen et al. 2009). The SEDs of these stars allow ages to be estimated via comparisons with isochrones, while their motions provide information about the central mass density. When combined, the spectrophotometric and positional information can be used to conduct tests of general relativity (e.g. Do et al. 2019). Studies of young stars near the GC also allow the mechanics of star formation in such an environment to be examined (e.g. Morris 1993; Ghez et al. 2003; Alexander 2005; Genzel et al. 2010).

The innermost regions of the Galaxy are structurally distinct from the Galactic bulge. The area surrounding the GC is part of the nuclear bulge (NB), which has been described by Launhardt et al. (2002). The gas and stars that make up the NB define a flattened structure that extends over  $\sim 230$  pc. The stellar content of the NB differs from that in the inner bulge, in that giants in the inner bulge appear to have uniformly old ages (Nogueras-Lara et al. 2018a), whereas some of the component stars of the NB are young.

At the center of the NB is the nuclear star cluster (NSC), which is a flattened structure with a half light radius of 4.2 pc (Schödel et al. 2014). Feldmeier-Krause et al. (2017a) examine the structural properties of the NSC and find a mass of  $2.1 \times 10^7 M_\odot$  within a 8.4 parsec sphere. They also measure a M/L ratio of 0.9, which is consistent with that in other nuclear star clusters. There are kinematic signatures suggesting that the NSC has grown at least in part by the accretion of massive star clusters (Feldmeier et al. 2014). The NSC lacks a central cusp defined by bright stars (Do et al. 2009; 2013), although fainter objects may define a cusp (Yusef-Zadeh et al. 2012; Gallego-Cano et al. 2018; Schödel et al. 2018). There is also a central concentration of ionized gas that is referred to as the GC mini-spiral

(e.g. Ekers et al. 1983; Tsuboi et al. 2016).

The NSC is a challenging observational target. Spectroscopic coverage is limited as heavy line-of-sight extinction effectively restricts studies to wavelengths longward of  $\sim 1\mu\text{m}$ , making traditional, well-calibrated spectroscopic probes of stellar content at visible wavelengths inaccessible. Crowding is an additional complication that limits the resolution of stars in the central parsec to  $K \leq 18$  (e.g. Davidge et al. 1997; Buchholz et al. 2009; Schödel et al. 2010, but see also Gallego-Cano et al. 2018). While the faint limit of current observations allows core helium-burning stars at the distance of the GC to be resolved, stars near the main sequence turn-off (MSTO) in color-magnitude diagrams (CMDs) of populations older than a few Gyr have yet to be sampled. Still, studies of resolved stars have revealed a broad range of ages with major recent star forming events within the past 10 Myr and at  $10^8$  years (e.g. Krabbe et al. 1995). While much of the stellar content by mass along the NSC sight line in the NIR has an old or intermediate age, young stars with solar or higher masses have a total mass of 14000 to 37000  $M_\odot$  (Lu et al. 2013).

Many of the recent studies that explore the stellar content near the center of the NSC have used AO-corrected IFU spectra, and almost all of these studies have examined the central parsec. A large population of early-type stars have been identified (Eisenhauer et al. 2005; Paumard et al. 2006; Do et al. 2009; Bartko et al. 2009, 2010), some of which have circumstellar dust shells (Eckart et al. 2013). The majority of early-type stars in the central arcsec are B main sequence stars, (Eisenhauer et al. 2005; Habibi et al. 2017). Young stars in the central parsec have a centrally-concentrated distribution (Paumard et al. 2006; Feldmeier-Krause et al. 2015), and outside of the central arcsec these define two disks that are kinematically distinct (Paumard et al. 2006; Bartko et al. 2009; 2010). The centrally-concentrated nature of the young stars is consistent with *in situ* formation (Feldmeier-Krause et al. 2015).

Do et al. (2013) find that the luminosity function of late-type stars near the center of the NSC is like that of the bulge. In contrast, the mass function of recently formed stars near the center of the NSC is top-heavy (Paumard et al. 2006; Bartko et al. 2010; Do et al. 2013; Lu et al. 2013). A top-heavy mass function can reconcile the observed X-ray emission with that expected from PMS stars (Nayakshin & Sunyaev 2005; Lu et al. 2013). Still, Bartko et al. (2010) find that within 0.8 arcsec of SgrA\* and at offsets in excess of 12 arcsec ( $\sim 0.5$  parsecs) young stars have a Salpeter mass function.

The early-type stars near the center of the NSC are likely not coeval, although there are uncertainties assigning ages. Paumard et al. (2006) and Bartko et al. (2010) suggest that the main population of bright early-type stars likely formed 6 Myr ago, while Lu et al. (2013) assign an age in the range 2.5 – 5.8 Myr. IRS 7, which is the most luminous star near the

GC, likely formed as part of a recent star-forming event, and Paumard et al. (2014) assign it an age of 6.5 – 10 Myr. There is also evidence for previous episodes of star formation during the past few tens of Myr as Bartko et al. (2010) find that the late-type B stars appear to be isotropically distributed, suggesting older ages. Star formation may also be occurring at the present day. Bartko et al. (2009) note that the shape of the disk and the mass distribution argues for *in situ* star formation, and Eckart et al. (2013) conclude that star formation near the center of the NSC is an ongoing process. Peiβker et al. (2020) discuss the properties of moderately faint ( $K \sim 18$ ) sources that have a thermal SED, and are identified as possible PMS objects close to SgrA\*. That star formation is on-going is consistent with the presence of gas flows and isolated dust structures near SgrA\* (e.g. Paumard et al. 2004).

The current wealth of imaging and spectroscopic studies have only sampled the tip of the stellar content iceberg. When working at their diffraction limits, the next generation of very large telescopes will resolve stars as faint as  $K \sim 22$  near the GC (e.g. Skidmore et al. 2015), and so the long-term prognosis for resolving the upper portions of the main sequence in old populations near the center of the NSC is positive. Still, achieving this goal is many years in the future. Even with the expected gains in angular resolution only a fraction of the stellar content will be examined, and it will not be possible to resolve main sequence stars with sub-solar masses within a few arcsec of SgrA\*.

Studies of integrated light provide a means of investigating the properties of all stars in a system, including the faint main sequence stars that define the mass function among low mass stars and fainter pre-main sequence objects, albeit in an encoded format. The problems associated with binarity in – say – counting stars to assess the mass function or interpreting CMDs is removed when examining integrated light, as there is an unbiased and complete sampling of all objects. The composite spectrum of the GC may also yield clues into the origins of the stars in the NSC through an examination of chemical mixtures; for example, did stars in the NSC form from gas that migrated inwards from the Galactic thin disk, or in dense massive star clusters that subsequently spiralled into the central regions of the Galaxy (e.g. Antonini et al. 2012; Arca-Sedda & Cappuzzo-Dolcetta 2014)? SEDS constructed from integrated spectra can also examine the influence that the GC environment has on stellar properties, testing the suggestion that some stars near SgrA\* have been stripped of their envelopes via stellar collisions (e.g. Alexander 1999; Genzel et al. 2003; Dale et al. 2009) or by interactions with dense proto-stellar clumps (Amaro-Seoane & Chen 2014), as this will result in a deficiency of spectroscopic signatures from cool evolved stars.

Studies of the integrated NIR spectrum of the NSC provide a direct means of assessing the properties of its component stars over a range of luminosities, while also identifying similarities between the GC, nearby galaxy nuclei, and star-forming regions in general. Inte-

grated spectra provide information that is complementary to that obtained from the imaging surveys of the inner Galaxy discussed earlier in this section. While individual bright stars can be resolved in the central parsec of the Galaxy, this is not yet possible for even the nearest galaxies. Spectra of the NSC thus provide a bridge that links the information obtained for the inner Galaxy to the nuclei of more distant systems, and provide a means of answering questions such as: Do the properties of the stars and star-forming regions near the center of the NSC differ from those in the rest of the Galaxy? and in other galaxies? Is the duty cycle of star-forming activity near the GC consistent with that in other galaxy nuclei? Is there evidence for ionization from sources other than the photospheres of hot stars?

Figer et al. (2000) discuss the integrated spectroscopic characteristics of the area within a few arcsec from SgrA\*. Using spectra that span 2 to  $2.4\mu\text{m}$ , they find that light within a few tenths of an arcsec of SgrA\* has characteristics that are consistent with those of early-type stars. Spectroscopic signatures of late-type stars, such as the first overtone CO bands, only become prominent at radii in excess of an arcsec from SgrA\*. However, the angular coverage of these data is very small.

Shields et al. (2007) discuss observations of emission line nuclei that were obtained for the Survey of Nearby Nuclei with STIS (SUNNS), and examine the GC in the context of those objects. As extinction makes recording the visible wavelength spectrum of the GC problematic, they estimate the  $\text{H}\alpha$  luminosity of the GC from free-free emission measurements, and conclude that it is comparable to that in the nuclear regions of most galaxies in the SUNNS sample. Furthermore, the absence of a strong compact X-ray source and the low-ionization state of lines suggests that the center of the NSC is neither a Seyfert nucleus nor a LINER. Rather, it appears to be an HII nucleus, or possibly a transition object.

There have been more recent studies of the inner Galaxy that use spectra of integrated light. Feldmeier et al. (2014) obtained integrated light spectra of a  $4 \times 3.5$  arcmin area that includes SgrA\*. This sky coverage was obtained using drift scanning techniques, and the angular resolution perpendicular to the slit is  $\sim 2$  arcsec. The primary scientific driver for these data was to examine kinematics, and the wavelength coverage was restricted to  $2.29 - 2.41\mu\text{m}$ , thereby sampling the three first overtone CO band heads. Feldmeier-Krause et al. (2015) obtained KMOS spectra in the  $K$ -band spectra of a  $65 \times 43$  arcsec area that includes SgrA\*. These data were used to examine the spectra of individual stars and also map the angular distribution of  $\text{Br}\gamma$ ,  $\text{HeI}$ , and  $\text{H}_2$  1–0 S(1) emission lines.

More direct comparisons with external nuclei have been made in the mid-infrared (MIR). Simpson et al. (1999) examine the strengths of MIR emission lines in central Galactic fields and find that they are similar to those in a low excitation HII region rather than an AGN. They note similarities with M82, pointing out that the diffuse radiation field inferred

from the line strengths are indicative of an aging starburst.

In the present paper long-slit spectra in the wavelength interval  $0.9 - 2.4\mu\text{m}$  that sample the central few parsecs of the NSC along its major axis are discussed. The spectra were recorded with the Flamingos-2 (F2) imaging spectrograph on Gemini South (GS). The use of a long slit permits coverage of parts of the NSC that are well outside of the central parsec, which has been the target of most previous spectroscopic studies. A wider range of wavelengths are also covered. The inclusion of spectra in the  $J$ -band are of particular use for identifying bright foreground disk stars that will otherwise contaminate the integrated spectrum. The NIR spectrophotometric properties of the NSC in four different angular intervals are compared with model spectra to gain insights into the chemical mixture of stars that span a range of evolutionary states, and assess the stellar and chemical homogeneity of the NSC. Comparisons are also made with other galactic nuclei.

Details of the observations and their reduction are discussed in Section 2. Basic characteristics of the spectra are examined in Section 3, while comparisons with model spectra are made in Section 4. Comparisons are made with spectra of galaxy nuclei in Section 5, where a spectrum of the young component near the GC is also extracted. A summary and discussion of the results follows in Section 6.

## 2. OBSERVATIONS & REDUCTIONS

The spectra were recorded with F2 (Eikenberry et al. 2004) on GS for program GS-2018A-Q-414 (PI: Davidge). The F2 detector is a Teledyne Hawaii-2  $2048 \times 2048$  array, and each pixel subtends  $0.18$  arcsec along the spatial direction. The dispersing elements are grisms.

There are challenges associated with obtaining a spectrum of the NSC that can be compared with model spectra and the nuclear spectra of other galaxies. Representative stellar content must be sampled to avoid stochastic effects. This is of particular relevance in the NIR, as much of the NIR light from systems that are older than a few Myr comes from intrinsically luminous highly evolved stars that have short evolutionary timescales. Such objects are susceptible to stochastic sampling effects, even in dense environments. Some of the stellar content near the center of the NSC also has a complicated projected distribution, with the youngest stars located in warped disks (e.g. Bartko et al. 2009; 2010). These sampling issues can be mitigated by observing moderately large areas at the expense of angular resolution. For this study spectra are constructed from areas that cover  $50 \text{ arcsec}^2$  in the central regions of the NSC, and  $65 \text{ arcsec}^2$  in the outer regions of the NSC.

The spectra were recorded with the JH and HK grisms, and so deliver a combined wavelength coverage of  $0.9 - 2.4\mu\text{m}$ . The slit used for these observations has a length of 4.3 arcmin and a width of 0.4 arcsec. The spectral resolution with this slit width varies between  $\frac{\lambda}{\Delta\lambda} = 500$  and 1100, depending on wavelength. The NSC has a half light radius of 4.2 pc (Schödel et al. 2014), which corresponds to  $\sim 110$  arcsec at the distance of the GC; the length of the F2 slit thus exceeds the half light diameter of the nuclear star cluster.

The slit was oriented to parallel the Galactic Plane (GP) for all observations. Two slit pointings centered on SgrA that are offset  $\pm 1$  arcsec perpendicular to the GP were observed to increase spatial coverage. The slit positions sample the areas of high  $\text{Br}\gamma$  and  $\text{HeI}2.06\mu\text{m}$  emission in the central regions of the NSC, as shown in Figures 7 and 8 of Feldmeier-Krause et al. (2015).

In order to remove the telluric and thermal emission that dominates the sky signal at these wavelengths it is desirable to sample areas of pristine sky. This is a challenge as the NSC is located in the Galactic bulge, and so observing completely blank sky fields requires pointing offsets of tens of degrees, thereby complicating efforts to obtain a reliable local background measurement. Fortunately, there are extended areas of very high extinction near the NSC that more-or-less monitor the background sky. Spectra of a high-opacity dust lane that parallels the GP were thus recorded. The dust lane is  $\sim 1$  arcmin to the south east of the GP. The locations of the science and background slits are shown in Figure 1.

Pockets of high extinction appear as lighter areas in Figure 1, and there are clear angular variations in the extinction in the direction of the NSC. The largest variations in extinction tend to occur perpendicular to the GP, with the areas of highest extinction being found at southern Galactic latitudes, which is the region where the background slit measurements are made. The positioning of the F2 slit was checked for large-scale extinction variations. While portions of the slit to the lower right of the GC in Figure 1 skirt areas of high extinction, the slit avoids these. While there are comparatively small areas along the slit where the signal dips to levels that are consistent with high levels of extinction, these do not dominate the overall signal. The impact that these small pockets of extinction might have on the spectrum are mitigated by observing two slit positions that are offset perpendicular to the GP.

Exposures of the NSC and the background dust lane were alternated in the sequence NSC – dust lane – NSC – dust lane etc. The NSC and dust lane observations were dithered by a few arcsec along the slit from exposure-to-exposure to mitigate against light from individual stars and cosmetic defects on the detector. In addition to the NSC observations, spectra of early-type stars were usually recorded at the beginning and end of a nightly observing session to monitor telluric absorption features. These were accompanied by exposures of a

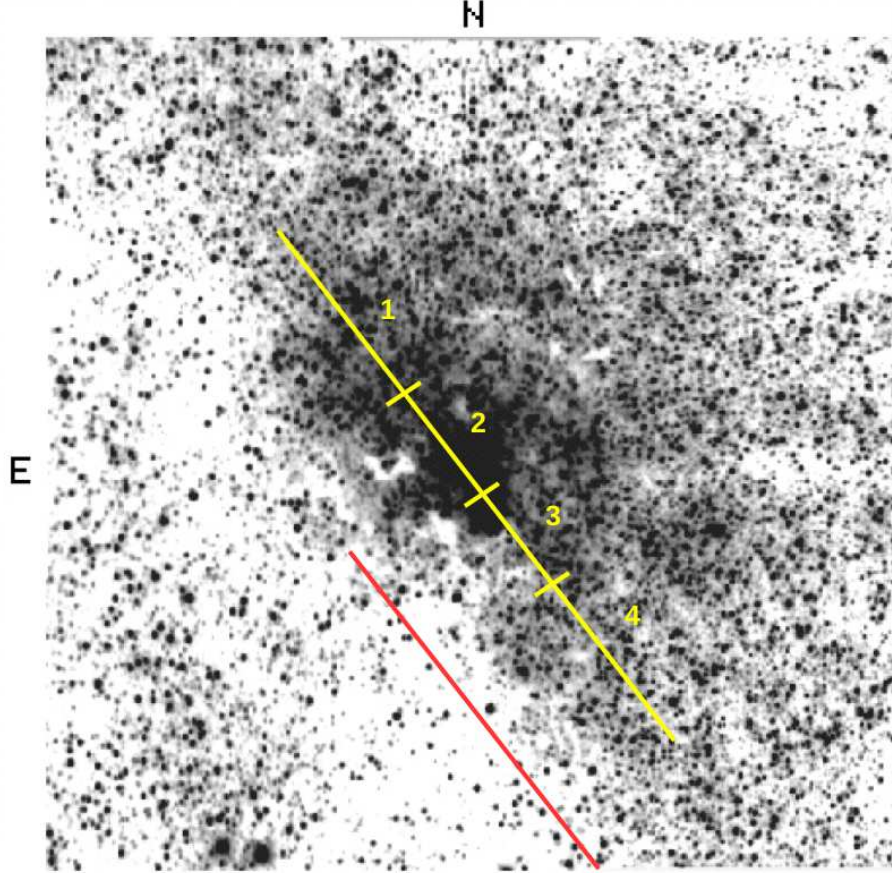


Fig. 1.— Slit locations. The background image is a  $6.2 \times 6.2$  arcmin  $K$  image centered on SgrA from Figure 1 of Davidge (1998). The NSC (yellow line) and background (red line) slit locations are indicated. While only one yellow line is shown, there are actually two NSC slit pointings that are offset by  $\pm 1$  arcsec perpendicular to the Galactic Plane. The background slit extends off of the image. The yellow hash marks demarcate the regions that are defined in Section 3, and these sample areas of  $50 \text{ arcsec}^2$  for each of Region 2 and 3, and  $65 \text{ arcsec}^2$  for each of Region 1 and 4. Regions 2 and 3 sample the densest regions of the GC mini-spiral and the center of the nuclear star cluster.



continuum and Ar emission arc lamps that are located in the Gemini calibration unit to provide flat-field and wavelength calibration information. Spectra were recorded on four nights, and a summary of these observations can be found in Table 1.

Instrumental and atmospheric signatures were removed from the spectra by applying a standard recipe for the reduction of NIR spectra. The basic steps are: (1) the subtraction of background spectra from the NSC spectra, (2) division by flat-field exposures, (3) geometric rectification to remove distortions that are introduced by the F2 optics, (4) wavelength calibration, and (5) division by the spectrum of a telluric calibration star. The processed spectra for each slit position were aligned to correct for dither offsets along the slit and then averaged together. The spectra from both NSC slit positions were then combined.

The spectra were normalized to a pseudo-continuum that was identified by fitting a low-order Legendre polynomial. An iterative rejection algorithm was applied to suppress emission and absorption features when identifying the pseudo-continuum. A low-order fit reduces the risk of artificially flattening broad molecular features, and can track the pseudo-continuum since the division by the telluric standard star (step 5, above) corrects for high order wavelength variations in optical response due to atmospheric transmission and the observing system (i.e. telescope and instrument optics).

### 3. CHARACTERISTICS OF THE SPECTRA

#### 3.1. IRS 7 and Systematic Effects

The red supergiant (RSG) IRS 7 is the most luminous star near the GC, and is sampled with the F2 spectra. IRS 7 has been well-studied, and so serves as a benchmark to assess systematic effects in the F2 spectra that might arise due to the observational set-up (e.g. spectral resolution) and subsequent processing (e.g. placement of the pseudo-continuum). Carr et al. (2000) find  $T_{eff} = 3500 \pm 50\text{K}$  for IRS 7, and assign it a near-solar  $[\text{Fe}/\text{H}]$ , although they also find non-solar CNO abundances that they attribute to deep mixing. Paumard et al. (2014) assign IRS 7 an effective temperature of  $3600 \pm 195\text{ K}$ . The effective temperature of IRS 7 thus agrees with that of the RSG  $\alpha\text{ Ori}$  ( $T_{eff} = 3600 \pm 66$ ; Haubois et al. 2009), and Carr et al. (2000) compare the IRS 7 spectrum with that of  $\alpha\text{ Ori}$ . Carr et al. (2000) conclude that  $[\text{Fe}/\text{H}]$  in  $\alpha\text{ Ori}$  is similar to that of IRS 7, but also find that the first overtone CO bands in IRS 7 are weaker than those in  $\alpha\text{ Ori}$ .

We compare the spectrum of IRS 7 extracted from the F2 observations with that of  $\alpha\text{ Ori}$  to assess possible systematic effects in the F2 spectrum. The spectrum of  $\alpha\text{ Ori}$  recorded

by Rayner et al. (2009) for the IRTF library was downloaded from the archive website,<sup>1</sup> smoothed, and re-sampled to match the spectral resolution and wavelength sampling of the IRS 7 spectrum. The result was normalized to a pseudo-continuum using the same procedure that was applied to all F2 spectra. The processed  $\alpha$  Ori spectrum is compared with the IRS7 spectrum in Figure 2.

The agreement between the IRS 7 and  $\alpha$  Ori spectra near the  $1.33\mu\text{m}$  MnI lines in the top panel of Figure 2 is excellent. However, the agreement between the two spectra degrades at wavelengths  $< 1.3\mu\text{m}$ . This is due to the lower signal level in the IRS 7 spectrum at these wavelengths, compounded by the challenges removing telluric emission lines from faint sources.

IRS 7 is heavily reddened ( $E(B-V) \sim 8$ ), raising the possibility of contamination from diffuse interstellar bands (DIBs), which could complicate comparisons with  $\alpha$  Ori. The wavelengths of DIBs in the  $J$ -band are indicated in the top panel of Figure 2. There is poor agreement between absorption features in the IRS 7 spectrum and the wavelengths of DIBs, although the DIB near  $1.32\mu\text{m}$  is a possible exception. Thus, DIBs are not responsible for the differences between the IRS 7 and  $\alpha$  Ori  $J$ -band spectra.

Moving to the middle and bottom panels, the first and second overtone CO bands in the IRS 7 spectrum are clearly weaker than those in  $\alpha$  Ori, in agreement with what was found by Carr et al. (2000). This is noteworthy since the deep nature and broad wavelength coverage of the first overtone CO bands cause these features to overlap at the spectral resolution of the F2 observations, making them susceptible to possible uncertainties in the placement of the pseudo-continuum. In contrast to the CO bands, the depths and widths of most atomic features in the two spectra more-or-less match at wavelengths between  $1.5$  and  $2.4\mu\text{m}$ , and this includes the NaI $2.21\mu\text{m}$  doublet and the CaI $2.26\mu\text{m}$  triplet. Neither of these features are resolved into their component lines at the wavelength resolution of the F2 spectra.

The depths of the NaI $2.21\mu\text{m}$  and CaI $2.26\mu\text{m}$  features in IRS 7 and  $\alpha$  Ori in Figure 2 agree to within 1 - 2 percent. This level of agreement is of interest as Sellgren et al. (1987), Terndrup et al. (1991), and Blum et al. (1996) found that NaI $2.21\mu\text{m}$  and CaI $2.26\mu\text{m}$  tend to be deeper in stars near the GC than in the solar neighborhood, and this includes IRS 7. Using high resolution spectra, Carr et al. (2000) find that the Na lines in the  $2.21\mu\text{m}$  Na doublet in IRS 7 and  $\alpha$  Ori are similar in strength. However, the depths of Sc, V, and CN lines that are at wavelengths similar to the NaI doublet differ from those in  $\alpha$  Ori, in the sense of being deeper in IRS 7. While the spectral resolution of the F2 spectra in the  $K$ -band is higher than in the Blum et al. (1996) spectra ( $\frac{\lambda}{\Delta\lambda} = 650$  vs. 570), this is not

---

<sup>1</sup>[http://irtfweb.ifa.hawaii.edu/spex/IRTF\\_Spectral\\_Library/](http://irtfweb.ifa.hawaii.edu/spex/IRTF_Spectral_Library/)

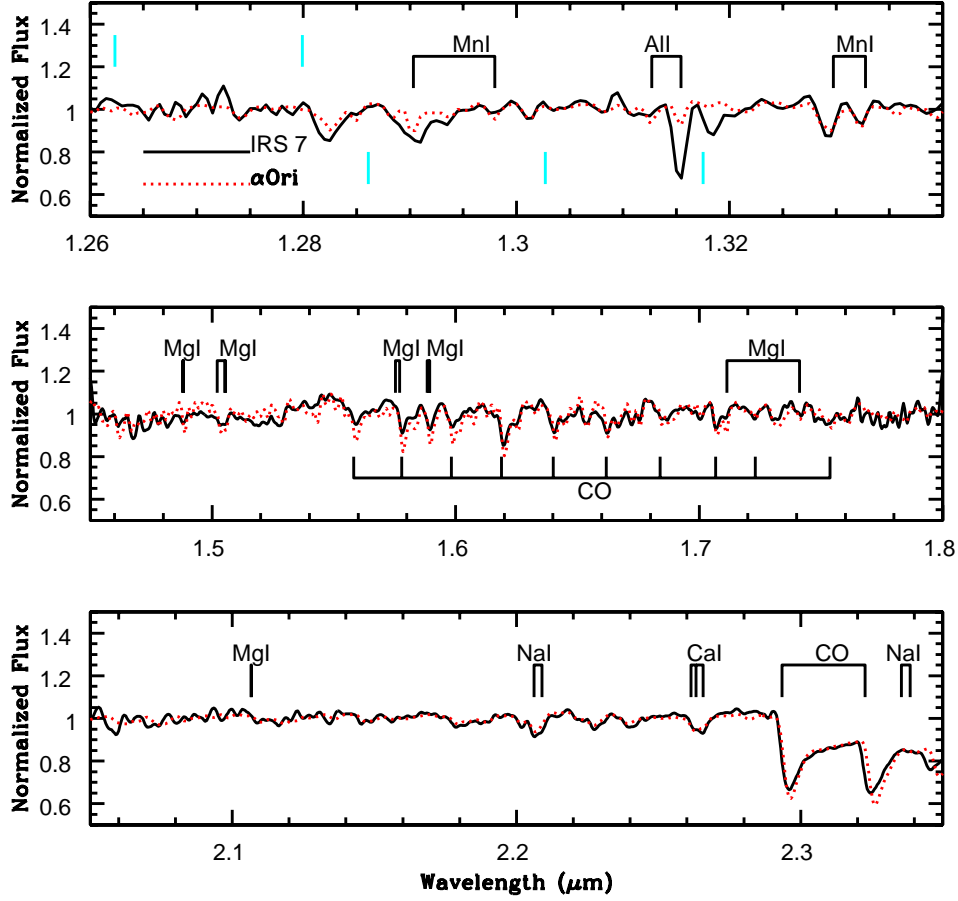


Fig. 2.— Spectra of IRS 7 (black line) and  $\alpha$  Ori (red dotted line). The IRS 7 spectra were extracted from the F2 observations, while the  $\alpha$  Ori spectra were constructed from a spectrum in the Rayner et al. (2009) library that was processed to match the spectral resolution and wavelength sampling of the IRS 7 spectra. The spectra of both stars have been normalized to a pseudo-continuum. The locations of diffuse interstellar bands (DIBs) in the  $J$ -band are marked with cyan lines in the top panel, and there is no obvious correspondence with features in the IRS 7 spectrum. Atomic and molecular features are identified using the rest frame vacuum wavelengths listed in Tables 7 and 10 of Rayner et al. (2009). There is good agreement between the strengths of most atomic features at wavelengths between  $1.3\mu\text{m}$  and  $2.3\mu\text{m}$ ; the agreement at wavelengths shortward of  $1.3\mu\text{m}$  degrades due to the lower S/N ratio of the IRS 7 spectrum at these wavelengths. The depths of the first- and second-overtone CO bands are shallower in the IRS 7 spectrum, in agreement with the relative strengths of the CO bands in the spectra of these two stars at higher spectral resolutions (Carr et al. 2000). Note that the depths of the NaI $2.21\mu\text{m}$  and CaI $2.26\mu\text{m}$  features in the IRS 7 spectrum match those in the  $\alpha$  Ori spectrum at the 1 – 2% level.

sufficient to resolve individual lines near  $\text{NaI}2.21\mu\text{m}$  (e.g. Figure 6 of Carr et al. 2000).

The placement of the pseudo-continuum may be responsible for the apparent discrepancy between the relative strengths of the  $\text{NaI}2.21\mu\text{m}$  and  $\text{CaI}2.26\mu\text{m}$  measurements in IRS 7 and  $\alpha$  Ori in the F2 spectra when compared with past studies. The wavelength region that contains the NaI and CaI lines coincides with  $\text{R}_2$  bands of CN. The F2 spectra have been processed by applying an unbiased and uniform algorithm for identifying continuum location that is based on broad wavelength coverage and is not sensitive to molecular absorption features or residuals from telluric emission/absorption features. In fact, the continuum levels in the IRS 7 and  $\alpha$  Ori spectra in the vicinity of the  $\text{NaI}2.21\mu\text{m}$  and  $\text{CaI}2.26\mu\text{m}$  lines in Figure 2 are in excellent agreement. Later in the paper it is shown that the  $\text{NaI}2.21\mu\text{m}$  and  $\text{CaI}2.26\mu\text{m}$  features in the integrated NSC spectra (1) vary with position along the F2 slit, and (2) are deeper than in models with a solar chemical mixture. Therefore, given the similar depths of  $\text{NaI}2.21\mu\text{m}$  and  $\text{CaI}2.26\mu\text{m}$  absorption in the IRS 7 and  $\alpha$  Ori spectra in Figure 2, if the F2 spectra systematically underestimate the depths of these features then the differences in line strengths that are discussed later in the paper are likely lower limits to actual differences.

### 3.2. Extraction of Spectra and Assessment of Stochastic Effects

Co-added spectra in four angular intervals have been considered to examine variations in the stellar content of the NSC along the slit, and the boundaries of these intervals are indicated in Figure 1. Regions 1 and 4 probe the outer regions of the NSC, while Regions 2 and 3 probe the center of the NSC and the GC Mini-spiral, which contains the youngest stars near the center of the NSC. While the use of wide angular gathers blurs spatial resolution, it boosts the S/N ratio while also suppressing the influence that individual bright stars might have on the spectra.

Each interval contains bright stars for which individual spectra can be traced. Some have blue SEDs, and stand out with respect to the majority of individual sources due to their high S/N ratios in the  $J$ -band. These are foreground stars, and light from these objects was removed prior to combining spectra in each region. Foreground star light was removed over the entire wavelength range in the angular interval where the PSF exceeded that of the surrounding background. The extraction area was filled by interpolating between the extraction limits.

The majority of individual stars in the F2 spectra have distinctive red SEDs. These are heavily reddened objects beyond the foreground Galactic disk, and the majority of these

objects are likely associated with the NSC, the NB disk, and the bulge. While much of the obscuration is in the foreground disk, there is also a dust component associated with SgrA (Davidge 1998). Still, the foreground disk extinction is more than sufficient to produce objects with highly reddened SEDs.

Individual bright stars can contribute significantly to the integrated light. IRS 7 is a prime example, and light from such objects can affect the integrated spectra. Two sets of spectra were thus constructed for each region. One includes all signal (but not that from foreground stars – see above) in each region. The other excludes light from all stars that have  $K < 12$ . Bright NSC stars were identified and their light removed using the same procedure described in the previous paragraph for foreground stars.

The  $K = 12$  threshold corresponds to a peak signal that departs from that of the unresolved body of light in the  $H$  and  $K$  spectra of Regions 2 and 3 at the  $2\sigma$  level. A fainter cut-off would have been defined in Regions 1 and 4, where the local background is substantially lower, and/or if the signal had been restricted to the  $K$ -band instead of both  $H$  and  $K$ . The RGB-tip occurs near  $M_K \sim -6.6$  for systems with near-solar metallicities (Ferraro et al. 2000), which corresponds to  $K \sim 10$  in the NSC. Therefore, the stars that are removed are not exclusively luminous young objects associated with recent star formation; rather, many are first or second ascent giants that likely formed Gyr in the past.

The seeing was  $\sim 1$  arcsec FWHM when these data were recorded, and so light from bright stars that are outside of the 0.4 arcsec slit will be present. This will occur most frequently in Regions 2 and 3, where crowding is most severe. Bright sources were identified solely from their appearance as extended objects in the slit spectra, and so light from very bright stars that are within 1 – 2 arcsec of the slit will still be identified, albeit with an amplitude that does not correspond to their actual brightness. Any light from bright stars that is missed is then at a level that is comparable to that from the main body of unresolved stars.

There are indications that contamination from bright stars that are within a few arcsec of the slit is not significant. Light that is dominated by a single bright star will have a lower velocity dispersion than that in the main body of stars. In fact, velocity dispersions measured in each region are found to increase when the light from bright stars is removed, as expected if the light is dominated by unresolved sources. In addition, the spectroscopic properties of each region changes when light from bright stars is removed, in the sense of features weakening after the removal of light from bright stars. This is most obvious in the CO(2,0) indices (see below), and is consistent with the successful removal of light from bright, late-type stars.

We conclude that while there might be residual contamination from the outer PSF wings of bright stars, it is at a level that is likely small when compared with the removal of light from stars that are detected on or close to the slit. Given that some contamination is present then the differences found here that are attributed to the removal of bright stars are likely lower limits. Spectra obtained with a higher angular resolution, where the contamination from light produced by bright stars off of the slit will be reduced, should then find even larger differences than those discussed below.

Region 2 includes IRS 7, which is by far the most luminous object near the GC ( $K \sim 7$ ,  $M_K \sim -9.5$ ), and is a star that contributes substantially to the total light from Region 2 in all three passbands. Given the brightness of IRS 7, the influence of bright stars on the integrated spectrum of Region 2 sets an upper limit to what is seen in the other regions, and so the Region 2 spectrum is examined in detail to provide a conservative means of assessing how light from bright stars affects the final spectra. The result of removing light from bright stars on the integrated spectra of Region 2 is explored in Figure 3, where spectra of Region 2 with and without light from resolved stars are compared.

The removal of bright stars alters the co-added spectrum in expected ways. The amplitudes of emission lines are boosted when light from bright stars is removed, as the subtraction of star light raises the fractional contribution made by nebular emission to the integrated light. Noise residuals that result from the subtraction of bright telluric emission lines are also amplified, and this is most obvious at the shortest wavelengths. The noise in the  $J$ -band spectrum reflects the inherent limitations to the removal of telluric lines from spectra of faint objects. Nevertheless,  $\text{Pa}\beta$  emission at  $1.282\mu\text{m}$  is clearly seen. Some deep absorption features at these wavelengths coincide with DIB transitions, although the comparisons in Figure 2 suggest that this may be fortuitous.

The dominant absorption features in the  $H$ -band are the second-overtone CO bands, and the depths of these do not change substantially when the light from bright stars is removed. This is perhaps not surprising, as these features are not sensitive to stellar color (e.g. Terndrup et al. 1991) and there is only a modest sensitivity to metallicity and effective temperature (e.g. Davidge 2020). In contrast, the depths of atomic features in the  $H$ -band weaken with the removal of light from bright stars, as expected if these lines are deeper in the spectra of evolved red stars.

Line indices measure the strengths of features in a quantifiable manner. Indices that measure the equivalent widths of  $\text{NaI}2.21\mu\text{m}$ ,  $\text{CaI}2.26\mu\text{m}$ , and  $\text{CO}(2,0)$  in Region 2 using the continuum and line wavelength intervals defined by Frogel et al. (2001) are listed in Table 2. Two entries are shown for each index: those measured from the spectra with only light from foreground stars subtracted, and those measured after light from all bright sources is

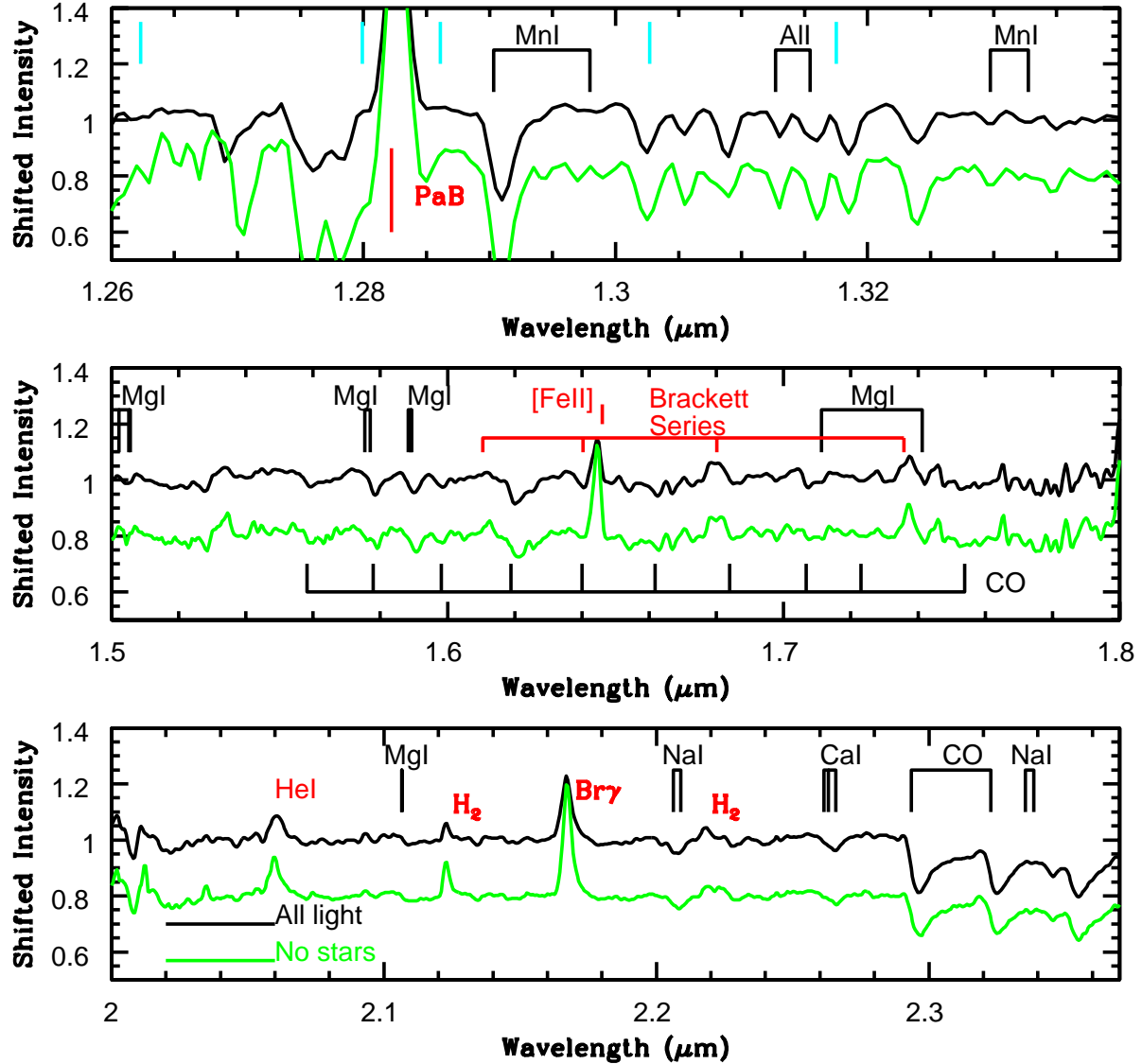


Fig. 3.— Assessing the influence of bright stars on the spectrum of Region 2. The black lines are spectra in which light from resolved bright stars is included, while the green lines are spectra where the light from bright sources has been removed. The spectra have been offset vertically for display purposes. Cyan lines in the top panel mark the expected locations of DIBs. The removal of light from bright stars (1) increases the relative strengths of emission lines, (2) decreases the S/N ratio, and (3) decreases the depths of many absorption features. However, the impact on the depths of absorption features may not be large, and the NaI2.21 $\mu\text{m}$  index changes by only a few tenths of an Å.

subtracted, with the latter measurements shown in brackets. The broad wavelength coverage of these indices makes them susceptible to contamination from atomic and molecular transitions that differ from those they are intended to explore. For example, Carr et al. (2000) show that the NaI2.21 $\mu$ m index is contaminated by Sc, V, and CN transitions. While there is then potential ambiguity in the features that are monitored, these indices still measure the depths of features of astrophysical interest in a uniform manner.

The indices in Table 2 are in an instrumental system, and so can not be compared directly with the measurements made by Frogel et al. (2001). The F2 spectra have a lower wavelength resolution than the spectra used by Frogel et al. (2001), and so it is likely that the indices measured from the F2 spectra are systematically smaller than those in the Frogel et al. (2001) system. The estimated  $2\sigma$  random uncertainties in these indices were estimated from column-to-column variances in the unbinned spectra coupled with the dispersion in signal within the continuum pass bands, and these are  $\pm 0.03\text{\AA}$  for NaI and CaI, and  $\pm 0.15\text{\AA}$  for CO(2,0). Given these uncertainties, there is thus a clear tendency for the equivalent widths measured from the spectra after the subtraction of bright stars to be systematically smaller than if only light from foreground stars is removed. Of the three indices considered, the NaI2.21 $\mu$ m index is the most robust in terms of sensitivity to bright stars, changing by only a few tenths of an  $\text{\AA}$  when the light from bright stars is subtracted. This conclusion also holds for NaI2.21 $\mu$ m indices measured in the other regions (see below).

### 3.3. Comparing SEDs Along the Slit

The  $H$  and  $K$  spectra of the four regions are compared in Figures 4 (light from bright stars included) and 5 (light from bright stars removed). We caution that the spectra in Figure 5 are likely not representative of composite stellar systems, as light from the brightest members has been removed, with the result that not all evolutionary states are sampled. The spectra of Regions 1 and 4 are noisier than those of Regions 2 and 3 due to lower light levels outside of the central regions of the NSC. The  $J$  band spectra of all regions except for Region 2, which is shown in Figure 3, have a low S/N ratio because of the high extinction towards the NSC, and so spectra at these wavelengths are not shown.

While these data were recorded at wavelengths where the extinction is greatly reduced when compared with shorter wavelengths, angular variations in extinction will still affect the light that is sampled. In particular, light from areas that have very high levels of foreground extinction will originate mainly from the foreground disk, which has a stellar content that likely differs from that of the inner Galaxy. As the foreground disk has a lower surface brightness than the central regions of the galaxy then these areas have conspicuous low



Date (UT; 2018)	Grism	$n_{exp}^a$
July 23	JH	$15 \times 120\text{sec}$
July 25	HK	$57 \times 15\text{sec}$
August 1	JH	$14 \times 120\text{sec}$
August 4	JH	$14 \times 120\text{sec}$

Table 1: Summary of Observations

<sup>a</sup>Number of SgrA exposures. A similar number of exposures were recorded of the background field (Section 2).

Region	NaI2.21 $\mu\text{m}^{a\ b}$ ( $\text{\AA}$ )	CaI2.26 $\mu\text{m}^{a\ b}$ ( $\text{\AA}$ )	CO(2,0) <sup>a\ c</sup> ( $\text{\AA}$ )
1	2.32 (2.05)	3.26 (3.23)	16.55 (14.19)
2	3.04 (2.69)	3.12 (2.07)	16.55 (11.11)
3	3.28 (3.12)	3.49 (3.07)	15.10 (13.89)
4	2.38 (2.09)	2.91 (2.50)	12.65 (11.84)

Table 2: Na, Ca, and CO Indices in Regions 1 – 4.

<sup>a</sup>All indices are in the instrumental system. Measurements made after light from bright stars is removed are shown in brackets.

<sup>b</sup>Estimated  $2\sigma$  uncertainty due to random errors is  $\pm 0.03\ \text{\AA}$ .

<sup>c</sup>Estimated  $2\sigma$  uncertainty due to random errors is  $\pm 0.15\ \text{\AA}$ .

light levels. Figure 1 of Davidge (1998) and Figure 32 of Nogueras-Lara et al. (2018b) demonstrate the variable nature of extinction near the NSC, and there are obvious areas where light originating from the inner regions of the Galaxy is blocked. The large-scale angular variations in line of sight extinction that are seen in the images presented by Davidge (1998) and Nogueras-Lara et al. (2018b) are not expected to be an issue for the present study, as the slit was positioned to avoid these. The areas of highest obscuration tend to occur to the south of the GP, which is where the background slit position is located. In contrast, the area sampled by the two F2 slit positions avoids large-scale areas of high extinction. While parts of Regions 3 and 4 come close to pockets of high extinction, obscuration is not evident in the light profile along the slit, confirming that areas of obscuration have been avoided.

Extinction maps constructed by Nogueras-Lara et al. (2018b) from the photometric properties of red stars indicate that there are extinction variations over angular scales  $\leq 10$  arcsec. Avoiding these small pockets of extinction is problematic although if – as indicated by the extinction maps of Nogueras-Lara et al. (2018b) – they occur in all four regions then they will bias the light along the entire slit by similar amounts. In fact, areas with very low light levels are found in isolated areas along the slit, and these have small angular extents, in agreement with the Nogueras-Lara et al. (2018b) extinction maps. The presence of such pockets of high extinction serves to diminish the total area covered in each region, rather than bias the total light coverage. Moreover, the affect of such regions in the current study is mitigated to some extent by the use of two F2 slit positions.

All four regions sample substantial amounts of light that originates from NSC stars. The light profile shown in Figure 14 of Schödel et al. (2014) indicates that Regions 1 and 4 each sample  $5 \times 10^4 L_{\odot}$ , while Regions 2 and 3 sample  $1 - 2 \times 10^5 L_{\odot}$ . These estimates are comparable to the light originating from a globular cluster. Furthermore, while there is contamination from non-NSC stars, the dense nature of the NSC means that contamination from these objects is modest in all four regions. This is evident from Figures 8 and 10 of Schödel et al. (2014) which demonstrate that the NSC in the areas sampled by the F2 slit is at least  $5\times$  brighter than non-NSC stars. Hence, while Regions 1 and 4 are more susceptible to contamination from non-NSC stars than Regions 2 and 3, the light in these regions is still dominated by NSC stars.

Region-to-region differences in the spectra are most noticeable in the K-band. The differences in the emission lines reflect the complex distribution of ionising sources and obscuring material throughout the inner Galaxy (e.g. Schödel et al. 2018; Ciurlo et al. 2016; Paumard et al. 2004; Ekers et al. 1983). Region-to-region variations in the  $K$ -band absorption spectrum have been quantified using the  $\text{NaI}2.21\mu\text{m}$ ,  $\text{CaI}2.26\mu\text{m}$ , and  $\text{CO}(2,0)$  indices, and these measurements are shown in Table 2. Systematic behaviour is seen in the

NaI2.21 $\mu$ m index in the sense that the index is larger in Regions 2 and 3 than in Regions 1 and 4. This trend is also seen when the spectra of the two slit positions are considered separately.

A comparison of the equivalent widths in Table 2 with the amplitudes of emission lines in Figure 4 indicates that the depths of absorption features do not vary in concert with emission line strength. This suggests that nebular continuum emission does not veil absorption features in the integrated spectrum. The absorption spectrum is then a viable probe of the stellar content.

If recent star formation near SgrA\* has proceeded for longer than a few Myr (e.g. Habibi et al. 2017) then some of the NIR light from Regions 2 and 3 will originate from a population of red objects that are cooler and have a lower surface gravity than the stars in Regions 1 and 4, with IRS 7 the most extreme example of such an object. Such evolved supergiants tend to have deep NIR absorption features. In fact, the equivalent width of NaI2.21 $\mu$ m is largest in Regions 2 and 3. However, the CaI2.26 $\mu$ m and CO(2,0) indices do not show a radial dependence with location along the F2 slit, suggesting that RSGs are not the dominant contributor to the light, which is consistent with the luminosity-weighted age estimate deduced from the SFH in Section 4.1.

Figure 5 shows spectra in which light from bright stars has been removed, and indices measured from those spectra are the entries in brackets in Table 2. There is a systematic variation in the depth of absorption features in Figure 5 and Table 2, in the sense that NaI2.21 $\mu$ m has a larger equivalent width in Regions 2 and 3 than in Regions 1 and 4, paralleling what was found in the spectra that included light from bright stars. That NaI2.21 $\mu$ m is deeper in the central regions of the NSC is thus a robust result. In contrast, Region 1 has the largest CaI2.26 $\mu$ m and CO(2,0) indices when light from bright stars is removed.

## 4. COMPARISONS WITH MODEL SPECTRA

### 4.1. The Models

There has been much recent work on the development of model spectra of simple stellar populations (SSPs) in the NIR (e.g. Maraston 2005; Conroy & van Dokkum 2012; Rock et al. 2016). However, there remain uncertainties in the physics of the highly evolved stars that contribute a significant fraction of the NIR light, and these uncertainties can have a profound impact on the SFH deduced solely from NIR spectra (e.g. Dahmer-Hahn et al. 2018). The inclusion of evolution in interacting binary systems can also significantly affect age estimates (e.g. Stanway & Eldridge 2018).

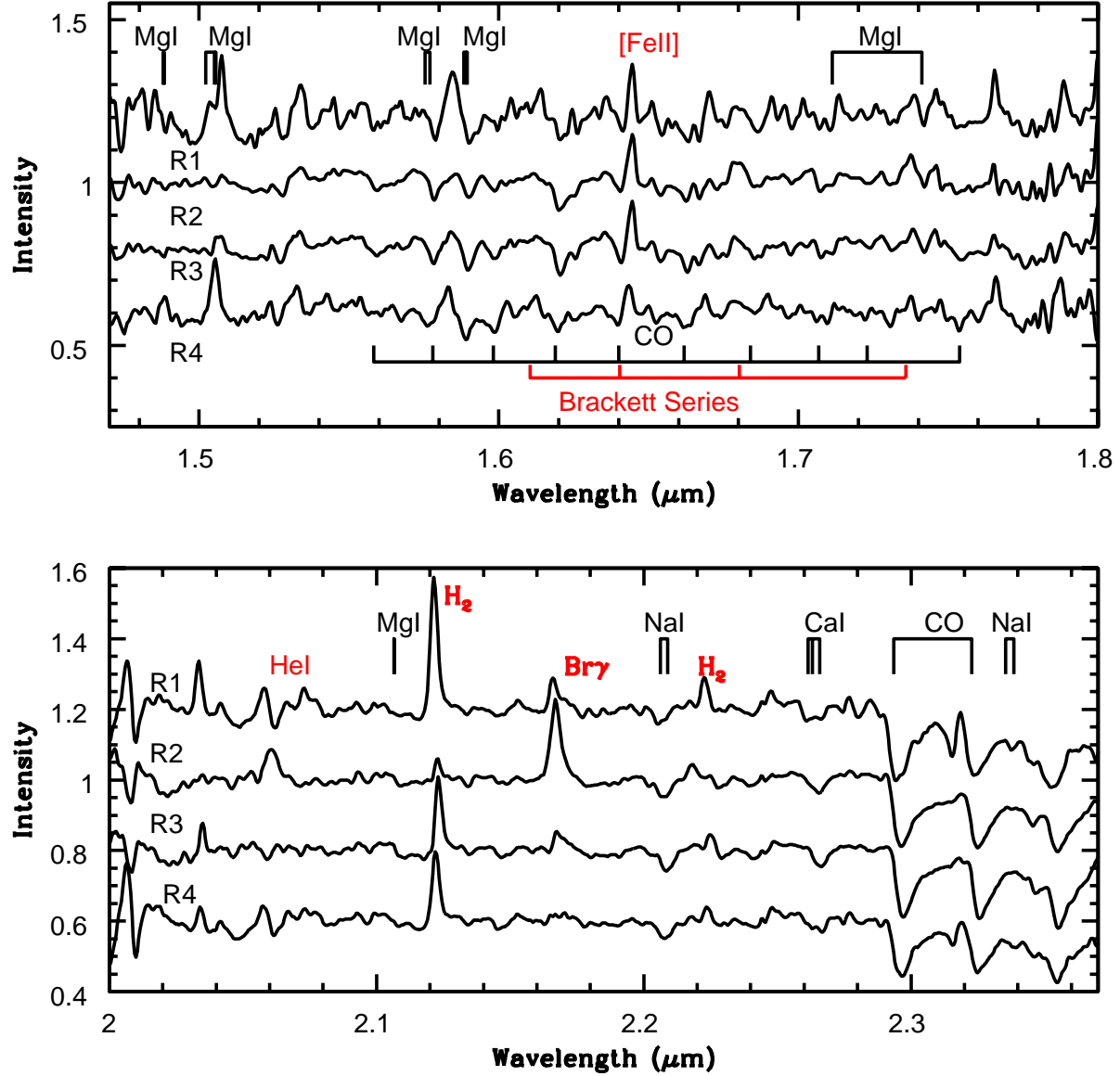


Fig. 4.— *H* and *K* Spectra of the four regions with light from bright resolved stars included. The spectra have been offset vertically for display purposes. Low S/N ratios prevent obtaining useable spectra in the *J*–band for three of the four regions, and the *J* spectrum of Region 2 is shown in Figure 3. All four regions sample part of the NSC, while Regions 2 and 3 also sample the GC Mini-spiral. The equivalent widths of emission lines vary from region-to-region, reflecting the complex distribution of ionizing sources in the NSC. Emission line strength and the depth of absorption features appears not to be correlated, suggesting that nebular continuum emission does not contribute significantly to the light at these wavelengths – the absorption spectrum thus probes the characteristics of the stellar content. The deepest absorption features tend to occur in Regions 2 and 3.

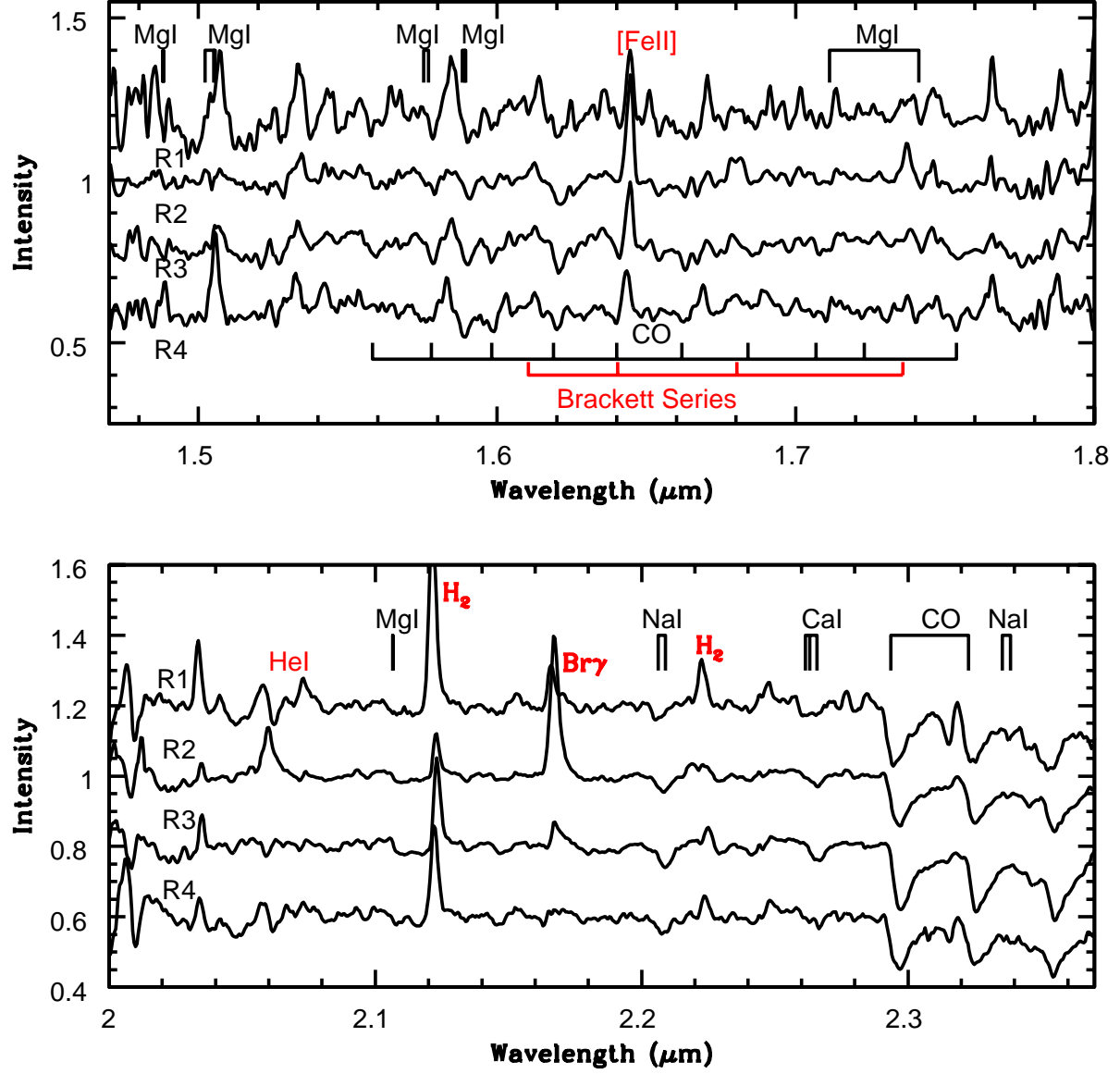


Fig. 5.— Same as Figure 4, but showing spectra in which light from the brightest stars has been removed.

The library of available stellar spectra is of obvious importance when generating model spectra. The IRTF library compiled by Rayner et al. (2009) is the basis for many SSP models, and in its original form it did not include stars with spectral-types earlier than A0 or a large set of objects with non-solar metallicities and chemical mixtures. These limitations complicated efforts to model the NIR SEDs of systems that are younger than a few tenths of a Gyr and/or that have experienced chemical enrichment histories that differ from the solar neighborhood. Having access to spectra that cover a full range of the highly evolved objects that can contribute significantly to the NIR light is also important. For example, the spectra of C stars in the IRTF library may not track the full suite of C star characteristics (Davidge 2020). The IRTF library is being expanded to cover a larger parameter space (Villaume et al. 2017), while other independent libraries are also becoming available (e.g. Gonneau et al. 2020).

The models used here are from the E-MILES compilation (Rock et al. 2016), and were generated from the BaSTI isochrones (Pietrinferni et al. 2004; Cordier et al. 2007) with spectra at NIR wavelengths constructed from stars in the IRTF library. A Chabrier (2001) mass function has been adopted. Paumard et al. (2006), Bartko et al. (2010) and Lu et al. (2013) conclude that the mass function of young massive stars near the GC is flatter than that among similar stars in the Solar neighborhood. However, the luminosity-weighted age towards the center of the NSC is a few Gyr (see below). The mass function of recently formed stars is then not expected to be a major issue for the current study, as most of the light comes from stars with a lower mass than those examined by Paumard et al. (2006), Bartko et al. (2010) and Lu et al. (2013). The stars that dominate the light from systems with ages of a few Gyr have also likely been well-mixed throughout the NSC – any localized variations in the mass function would then have been smoothed out.

A forward modelling approach is adopted for this study. Luminosity-weighted ages and metallicities have been found using results from studies of resolved stars near the GC. Figure 14 of Pfuhl et al. (2011) compares SFR measurements for the GC from various studies, and a hand-fit SFR *vs* time relation from the entries in that figure, which is weighted towards old and intermediate ages, was adopted for computing luminosity-weighted ages.

While there have been other age estimates made since the Pfuhl et al. (2011) compilation was published, these are not expected to alter our results. For example, Lu et al. (2013) estimate an age of 2.8 or 3.9 Myr for the most recent episode of star formation, whereas the youngest entry in the Pfuhl et al. (2011) compilation is  $\sim 6 - 7$  Myr. However, given that the weighting of old and intermediate populations in the NIR is greater than that of young populations then the luminosity-weighted age is not sensitive to changes in age estimates for the youngest stars.

There is some uncertainty in the ages of bulge stars. Renzini et al. (2018) discuss recent photometric studies of bulge stars, and note that these tend to find a uniformly old age. In contrast, age estimates based on spectroscopic properties yield a significant intermediae age component among metal-rich bulge stars (e.g. Bensby et al. 2017). While this introduces uncertainty in the luminosity-weighted age, this should not affect the task at hand, as the NIR SEDs of systems older than a few Gyr change only slowly with age. In the next section it is shown that the NaI2.21 $\mu$ m and CaI2.26 $\mu$ m indices have only a modest sensitivity to system age.

The integrated NIR luminosity of stars in various time intervals was found by assigning a M/L measurement to different age intervals. Figure 24 of Maraston (2005) summarizes  $K$ -band M/L ratios from various studies. There are not substantial model-to-model variations in the M/L ratios in that figure except near  $\sim 1$  Gyr. This age is where the fractional contribution from AGB stars to the NIR light is expected to be significant, and the dispersion in M/L ratios at this age in Figure 24 of Maraston (2005) are due to different approaches that were adopted to track AGB evolution. The uncertainties in M/L ratios near 1 Gyr do not introduce major uncertainties when generating luminosity-weighted ages in the NIR as the SFR in Figure 14 of Pfuhl et al. (2011) is comparatively low near 1 Gyr. Adopting the Pfuhl et al. (2011) SFH and Maraston (2005) M/L ratios then the luminosity-weighted age along the SgrA sight line is  $\sim 3$  Gyr.

As for luminosity-weighted metallicity, there is evidence for a preponderance of super-solar metallicity stars near the center of the NSC, although with a broad range of metallicities. Rich et al. (2017) discuss metallicity estimates of NSC giants and find a moderate spread in metallicity among older stars, with a mean  $[\text{Fe}/\text{H}] \sim -0.3$ . Cunha et al. (2007) find that young stars near the GC have a mean  $[\text{Fe}/\text{H}] \sim +0.1$ . Feldmeier-Krause et al. (2017b) examine the spectra of stars in the central 4 pc<sup>2</sup>, and find a wide distribution with a peak near  $[\text{M}/\text{H}] = +0.3$  dex, while Nandakumar et al. (2018) also find a peak metallicity +0.3 dex among stars near the GC. The stars observed for the latter study have  $K$  between 11 and 12, and are thus among the objects that are subtracted from the spectra throughout this work to examine luminosity effects. Schultheis et al. (2019) compile results from a number of studies and conclude that stars near the GC have super-solar metallicities while those in the inner bulge have a peak metallicity near solar. Given this diversity, models are considered here that have slightly super-solar metallicities, although slightly sub-solar metallicity models are also considered to examine the dependence of the results on the assumed metallicity, as well as possible systematic effects in metallicity estimates that may occur among M giants (Thorsbro et al. 2018). A scaled-solar chemical mixture is assumed.

## 4.2. Comparisons with Observations

Model spectra of a 3 Gyr SSP with  $[\text{Fe}/\text{H}] = -0.26$  and  $+0.06$  are compared with part of the  $K$ –band spectrum of SgrA in Figure 6. The models have been smoothed and re-sampled to simulate the wavelength resolution and cadence of the F2 spectra. The  $2.2 - 2.35\mu\text{m}$  wavelength interval was selected for comparison with the models as it contains a number of deep absorption features, is free of strong emission lines, and has a high S/N ratio when compared with other wavelengths.

NaI2.21 $\mu\text{m}$ , CaI2.26 $\mu\text{m}$ , and CO(2,0) indices were measured from the model spectra, and the results are listed in Table 3. Indices were measured from 1, 3, and 10 Gyr models with  $[\text{Fe}/\text{H}] = -0.25$  and  $+0.06$  to allow age and metallicity effects to be assessed. The entries in Table 3 indicate that the NaI2.21 $\mu\text{m}$  and CaI2.26 $\mu\text{m}$  indices are only mildly sensitive to changes in metallicity and age at the wavelength resolution of the F2 spectra, producing differences of only a few tenths of an Å over the age and metallicity ranges considered. Any differences between the observations and models larger than a few tenths of an Å are then likely not due to uncertainties in age and/or overall metallicity. The CO(2,0) index is more sensitive to changes in age and metallicity than either NaI2.21 $\mu\text{m}$  and CaI2.26 $\mu\text{m}$ . Indices were also measured in spectra with  $\frac{\lambda}{\Delta\lambda} \sim 400$ , which is lower than the resolution of 650 in the F2  $K$ –band spectra, and the NaI2.21 $\mu\text{m}$  and CaI2.26 $\mu\text{m}$  indices measured from the lower resolution spectra differ by only a few hundredths of an Å from those in Table 3.

Previous efforts to model the NaI2.21 $\mu\text{m}$  and CaI2.26 $\mu\text{m}$  features in the spectra of massive spheroids underestimated their strengths (e.g. Alton et al. 2018). Galaxy-to-galaxy variations in the equivalent width of NaI2.21 $\mu\text{m}$  have also been found (e.g. Rock et al. 2017, and others), suggesting that this index may be influenced by parameters other than age and metallicity. Although deep NaI2.21 $\mu\text{m}$  features are most commonly associated with massive spheroidal galaxies, these are also seen in lower mass early-type disk galaxies (Davidge 2020). Differences in  $[\text{Na}/\text{Fe}]$ , the nature of the mass function at the lower end of the main sequence, and variations in  $[\text{C}/\text{Fe}]$  (e.g. Rock et al. 2017; Sarzi et al. 2018) have been forwarded as possible causes of the galaxy-to-galaxy variations in the NaI2.21 $\mu\text{m}$  feature in integrated spectra.

The NaI2.21 $\mu\text{m}$  equivalent widths obtained from spectra of Regions 1 and 4 in which light from bright stars is included fall within the range defined by the models. However, the NaI2.21 $\mu\text{m}$  indices in Regions 2 and 3 are  $0.7 - 1.0\text{Å}$  larger than in the 3 Gyr models. The CaI2.26 $\mu\text{m}$  indices in all four regions are uniformly larger than in the models, which is consistent with what is seen in other galaxies (e.g. Alton et al. 2018; Davidge 2020). When light from bright stars is removed from the spectra then the NaI2.21 $\mu\text{m}$  indices for Regions 2 and 3 are still  $0.4 - 0.8\text{Å}$  deeper than in the 3 Gyr models. The equivalent width



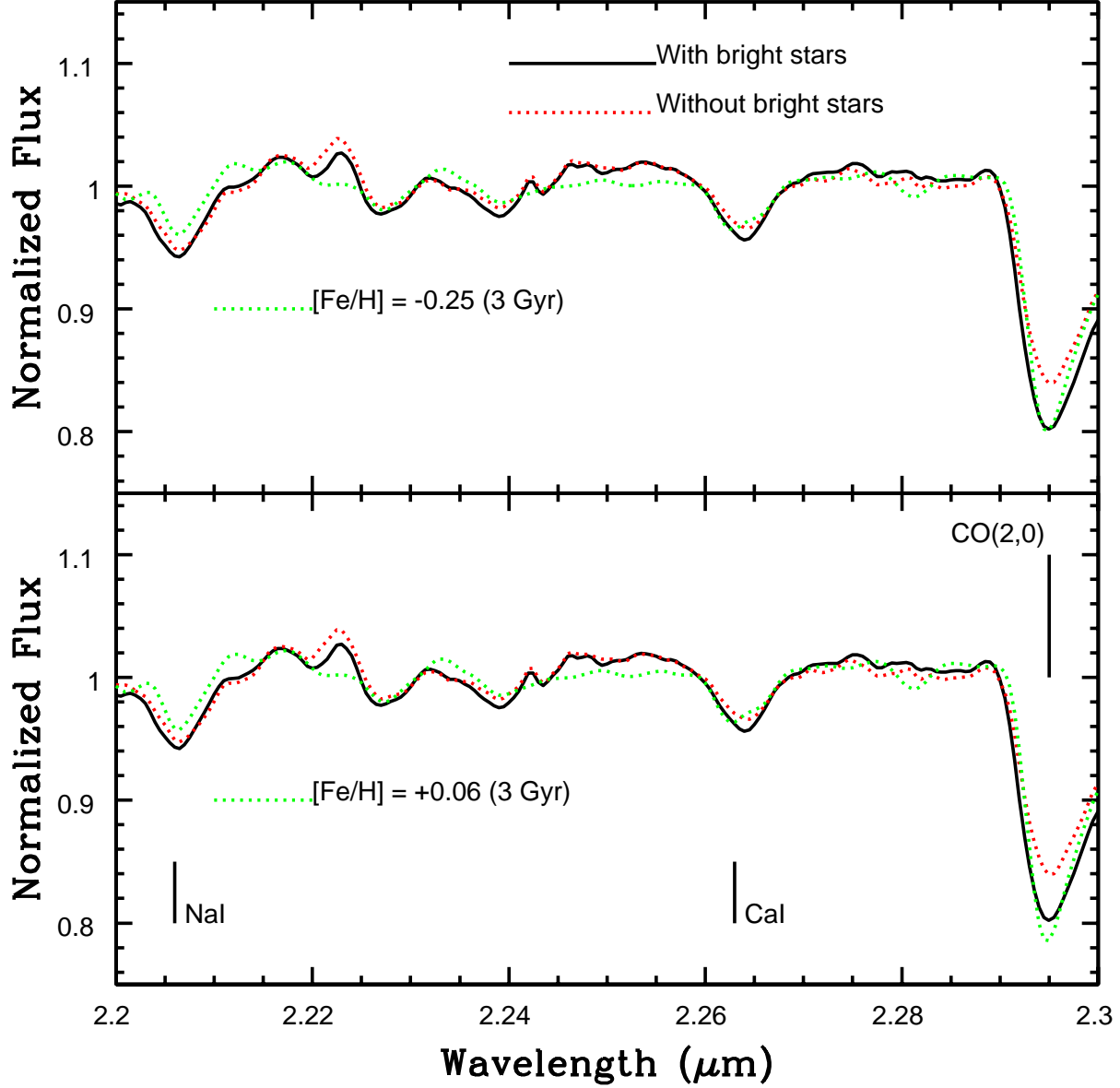


Fig. 6.— Model spectra of SSPs with  $[\text{F}/\text{H}] = -0.25$  (top panel) and  $+0.06$  (bottom panel) and an age of 3 Gyr are compared with the mean spectrum of Regions 2 and 3. The black line shows spectra in which light from bright stars has been retained, while the red dashed line shows the spectrum with this light removed. The  $2.2 - 2.35\mu\text{m}$  wavelength interval is free of strong emission lines, and so is well-suited for comparisons with model spectra.

Model	NaI2.21 $\mu\text{m}$ <sup>a b</sup> ( $\text{\AA}$ )	CaI2.26 $\mu\text{m}$ <sup>a b</sup> ( $\text{\AA}$ )	CO(2,0) <sup>a c</sup> ( $\text{\AA}$ )
–0.25 1 Gyr	2.08	2.01	11.58
+0.06 1 Gyr	2.13	2.12	12.04
–0.25 3 Gyr	2.16	2.18	13.27
+0.06 3 Gyr	2.31	2.35	14.18
–0.25 10 Gyr	2.29	2.40	14.05
+0.06 10 Gyr	2.44	2.46	14.25
NGC 4491	2.62	2.18	15.58

Table 3: Na, Ca, and CO Indices in Model Spectra and NGC 4491

<sup>a</sup>All indices are in the instrumental system. Those made with light from bright stars removed are shown in brackets.

<sup>b</sup>Estimated  $2\sigma$  uncertainty due to random errors is  $\pm 0.03 \text{ \AA}$ .

<sup>c</sup>Estimated  $2\sigma$  uncertainty due to random errors is  $\pm 0.15 \text{ \AA}$ .

of  $\text{CaI}2.26\mu\text{m}$  also drops when the light from bright stars is removed, but is still larger than predicted by the models for three of the four regions. In summary, the differences between the depths of the  $\text{CaI}2.26\mu\text{m}$  and  $\text{NaI}2.21\mu\text{m}$  features and the model measurements can not be attributed solely to stars with  $K < 12$ .

With the exception of Region 4, the  $\text{CO}(2,0)$  indices measured from the F2 spectra with light from bright stars included are uniformly deeper than those measured from the SSP model spectra. When light from bright stars is removed then the  $\text{CO}(2,0)$  indices are consistent with those in the model spectra. The bright stars that were removed when constructing the SgrA spectrum in Figure 6 are the most luminous, highly evolved objects in the field, and thus typically should have deep CO bands, although we recall that the CO indices in IRS 7 are *weaker* than found in  $\alpha$  Ori. To the extent that the spectra can be represented by a luminosity-weighted age and metallicity then the SSP models considered here thus underestimate the contribution from  $\text{CO}(2,0)$  in the spectrum of bright stars. An alternative is to assume that the spectra have a luminosity-weighted metallicity that is  $\sim 0.6 - 0.7$  dex, but this is not consistent with the metallicity estimates for individual stars discussed in Section 3. A possible explanation for these results is that the chemical mixture of stars in the NSC may not match those in the solar neighborhood.

Sellgren et al. (1987) and Blum et al. (1996) find that the  $\text{NaI}2.21\mu\text{m}$  and  $\text{CaI}2.26\mu\text{m}$  absorption features are deeper in the low resolution spectra of stars in the NSC than in the spectra of solar neighborhood counterparts, and the measurements made from the F2 spectra are consistent with this. While this might point to super-solar  $[\text{Na}/\text{Fe}]$  and  $[\text{Ca}/\text{Fe}]$  in these stars, Carr et al. (2000) find that the  $\text{NaI}2.21\mu\text{m}$  index is contaminated by lines of V, Sc, and CN at low wavelength resolutions, and that it is those lines that are driving differences in the depths of the  $\text{NaI}2.21\mu\text{m}$  index in IRS 7 and  $\alpha$  Ori. This opens the possibility that elements other than Na might explain the difficulty matching the depths of  $\text{NaI}2.21\mu\text{m}$  (Alton et al. 2018, but see also Rock et al. 2017) in the spectra of early-type galaxies.

The comparisons in Tables 2 and 3 indicate that deep  $\text{NaI}2.21\mu\text{m}$  absorption is not restricted to cool giants in the NSC, but is also seen in integrated light that samples a large range of evolutionary states and effective temperatures, as the  $\text{NaI}2.21\mu\text{m}$  and  $\text{CaI}2.26\mu\text{m}$  indices are larger than expected even after light from luminous bright stars is removed.  $\text{NaI}2.21\mu\text{m}$  and  $\text{CaI}2.26\mu\text{m}$  equivalent widths that are larger than predicted by the models must then occur in stars that span a wide range of evolutionary states. This could occur if there are systematic differences in chemical mixture between stars near the center of the NSC and in the solar neighborhood.

The existence of non-solar chemical mixtures among GC stars is a matter of controversy. Do et al. (2018) find deeper than expected Sc lines in the spectra of M giants in the NSC,

and interpret this as evidence for a non-solar chemical mixture. However, Thorsbro et al. (2018) argue that the formation of these lines in the photospheres of cool stars is not well understood. Nevertheless, the differential comparison conducted by Carr et al. (2000) of the spectra of IRS 7 and  $\alpha$  Ori, which are stars that have similar effective temperatures and surface gravities, point to clear differences in the depths of lines of Sc, V, and CN.

Non-solar chemical mixtures would indicate that the bulk of the stars along this line of sight formed from material that did not experience evolution in a thin disk-like environment. Rather, they may have formed from material that was enriched very quickly, with only minimal subsequent dilution over long time scales. Alternatively, it could also indicate an IMF that differs from that in the solar neighborhood. The Na abundance of stars in globular clusters show systematic effects that differ from those of stars in open clusters (e.g. Gratton et al. 2012; Cunha et al. 2015), and the chemical evolution of globular clusters might then yield clues for understanding the non-solar mixtures that may occur near the GC.

## 5. THE SPECTRUM OF THE CENTER OF THE NSC

### 5.1. Comparisons with the Spectra of Other Galaxies

Neumayer et al. (2020) review the properties of the Galactic NSC in the context of nuclear clusters in other galaxies. They conclude that the NSC is a typical nuclear cluster in terms of spatial extent, mass, and shape. The stellar content of the NSC is also consistent with that of other late-type galaxies, in the sense that there is a broad range of ages that extend from young to old populations.

The spectrum of the NSC contains a fossil record of its SFH. Given that the NSC has similar properties to the nuclear clusters in other galaxies then it is perhaps not surprising that the integrated NIR spectrum of the NSC has characteristics that are similar to those of nuclei in other galaxies. Evidence to support this claim can be found in Figures 7 and 8 where the mean spectrum of Regions 2 and 3 (hereafter referred to as the SgrA spectrum) is compared with the nuclear spectra of the Sc galaxy NGC 7793 (Davidge 2016), and the star burst galaxy NGC 253 (Davidge 2016). These galaxies represent two distinct types of late-type galaxies. NGC 7793 is a nearby Sc galaxy, with on-going star formation throughout its disk. While the nucleus of NGC 7793 contains stars younger than  $\sim 100$  Myr (Kacharov et al. 2018), its NIR spectrum lacks prominent emission lines. The presence of an inverse color gradient also hints at a complicated formation history for its nucleus (Kacharov et al. 2018). NGC 253 is a barred Sc galaxy, and is one of the nearest starburst galaxies, with vigorous star formation occurring throughout.

Nuclear star clusters are found over a broad range of Hubble types (e.g. Seth et al. 2008). To enable a comparison with a nuclear cluster that is not in a late-type disk galaxy, spectra of the Virgo cluster early-type disk galaxy NGC 4491 (Davidge 2020) is also shown in Figures 7 and 8. NGC 4491 is an SBa(s) galaxy in the Virgo cluster that has little or no on-going star formation in its disk, but has a blue nuclear SED at visible wavelengths and a red nuclear SED in the MIR (Davidge 2018). It is the only early-type galaxy in the sample discussed by Davidge (2020) that has NIR line emission, and has a near-solar central metallicity (Davidge 2018). Moreover, the  $\text{NaI}2.21\mu$  and  $\text{CaI}2.26\mu\text{m}$  features in the NGC 4491 spectrum are deeper than predicted by models, as is the case in Regions 2 and 3.

The spectra in Figures 7 and 8 sample a range of spatial scales that exceed the area covered with the F2 spectra. The NGC 253 spectrum covers a region with an 8 parsec radius, while the NGC 7793 spectrum samples an area with a 16 parsec radius. The NGC 4491 spectrum covers an  $80 \times 80$  parsec area.

The  $H$ –band spectra in Figure 7 have a range of characteristics. The emission spectrum of NGC 253 IRC in the  $H$ –band is dominated by [FeII] and Brackett lines, and these have much larger equivalent widths than in the other nuclei, indicating a much younger luminosity-weighted age. Still, the absorption features in the NGC 253 IRC  $H$ –band spectrum match those in the other systems. There is weak line emission in the NGC 7793  $H$ –band spectrum, indicating that there has not been extensive levels of star formation within the past few Myr in the central few parsecs of that galaxy. The depths of absorption features in the  $H$ –band spectrum of NGC 7793 match those in the SgrA spectrum. Emission lines in the NGC 4491 spectrum are intermediate in strength between those in NGC 253 and NGC 7793, and come closest to matching those in SgrA. The  $H$ –band absorption spectra of NGC 4491 and SgrA spectra also agree.

There are clear differences between the  $K$ –band spectra of the nuclei in Figure 8. The first-overtone CO bands in the NGC 7793 spectrum are markedly deeper than in the SgrA spectrum, suggesting that there is a larger fractional contribution from cooler, low surface gravity stars to the NIR light in the central few parsecs of NGC 7793 when compared with the central parsec of SgrA. The luminosity-weighted age in the region sampled by the NGC 7793 spectrum is thus substantially younger than in the F2 NSC observations. While the depths of absorption lines in the SgrA and NGC 253 spectra more-or-less agree, the emission lines in the NGC 253 spectrum have larger equivalent widths.

The similarities between the SgrA and NGC 4491 absorption spectra in Figures 7 and 8 are not surprising considering that the luminosity-weighted age and metallicity estimates for the SgrA line of sight found in Section 4 agree with those deduced from the integrated spectrum of NGC 4491 by Davidge (2018), who based that estimate on absorption features

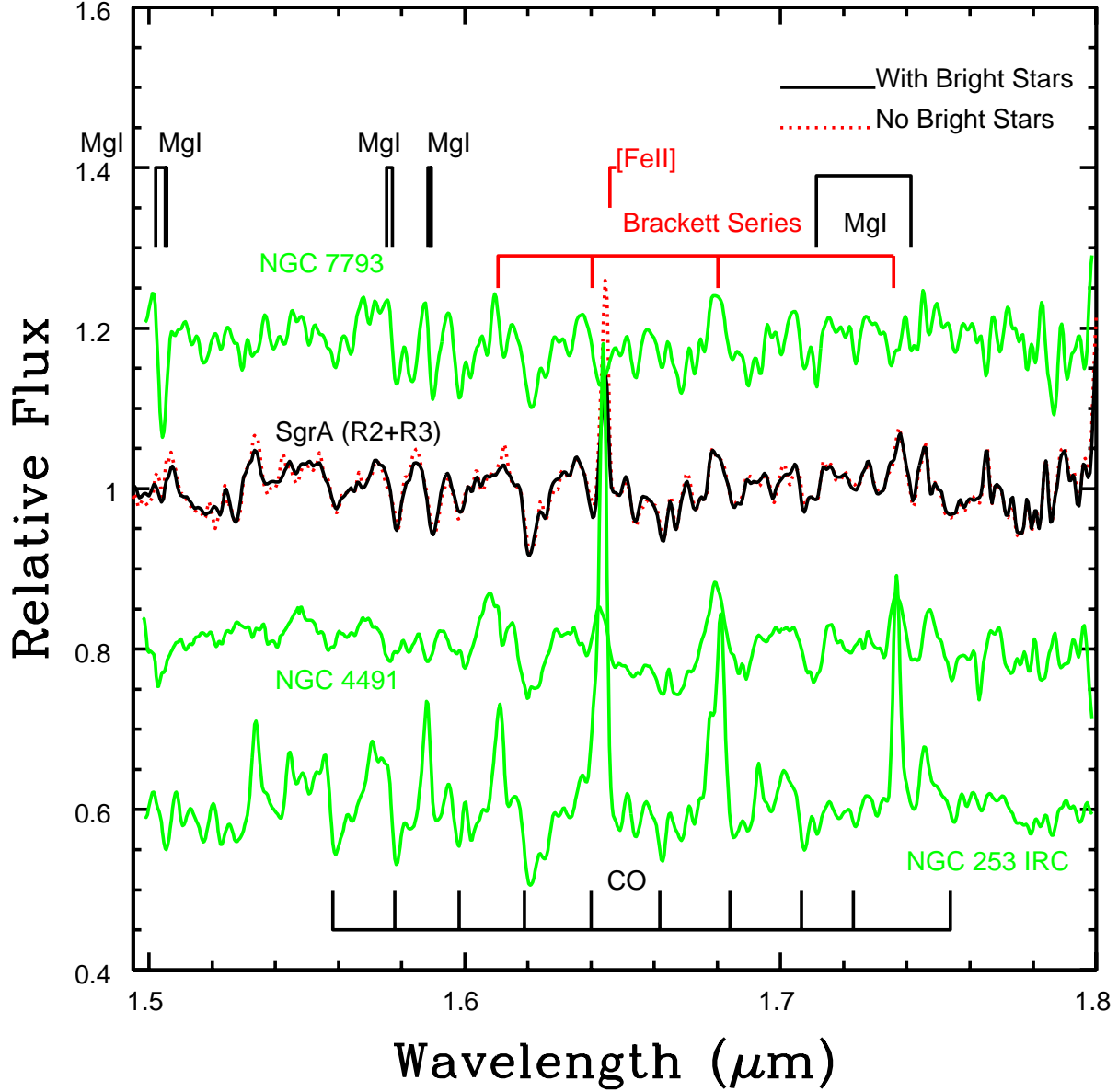


Fig. 7.— Comparing the mean  $H$ -band spectrum of Regions 2 and 3 (hereafter referred to as the ‘SgrA spectrum’) with the spectra of extragalactic nuclei that host current or recent star formation. The black line shows the continuum-normalized SgrA spectrum with light from bright stars retained, while the dashed red line shows the spectrum with light from bright stars removed. The green lines show the spectra of NGC 7793 (Davidge 2016), NGC 253 IRC (Davidge 2016), and NGC 4491 (Davidge 2020). The SgrA and NGC 4491 spectra have similar appearances.

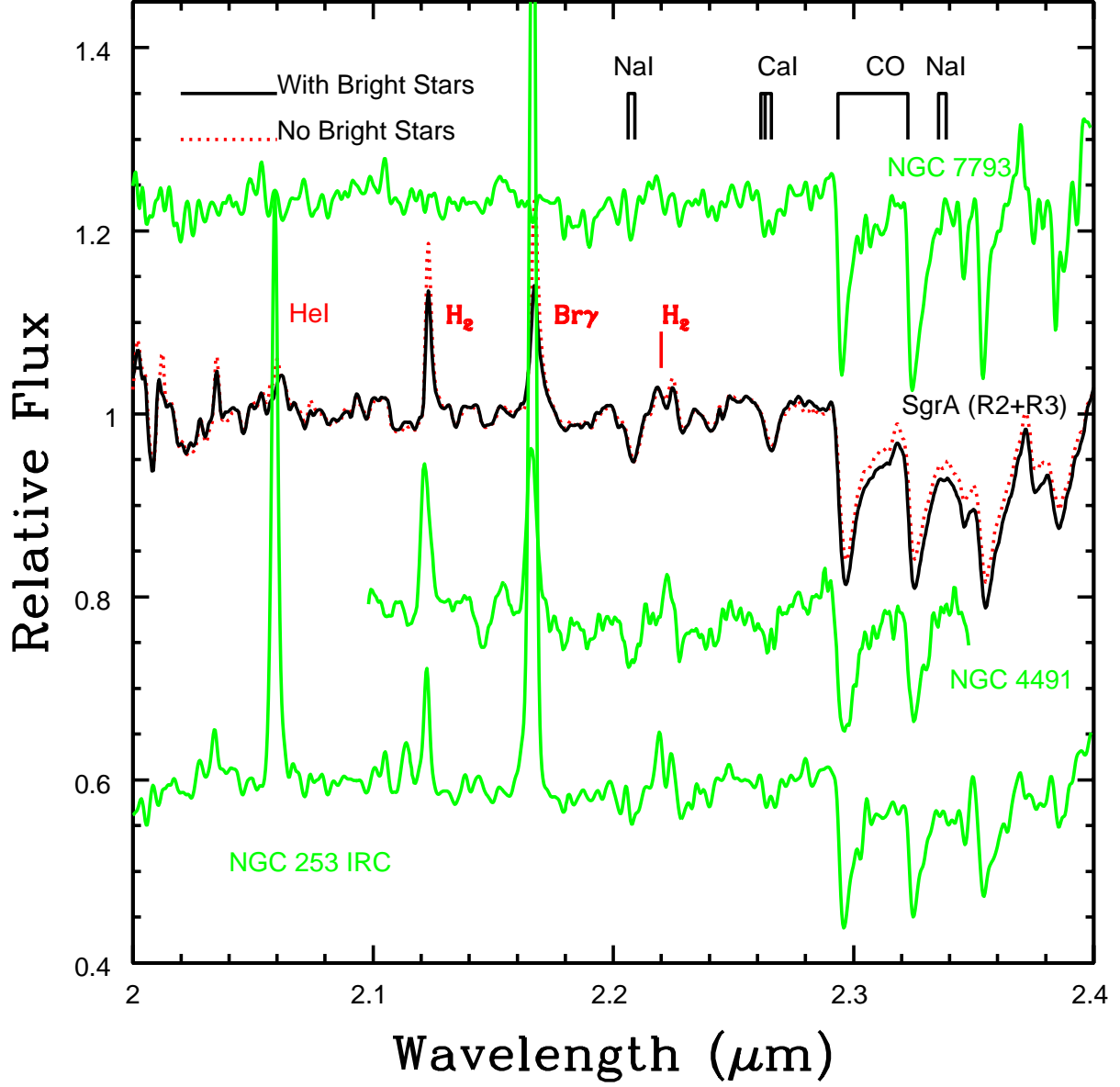


Fig. 8.— Same as Figure 7, but with  $K$ -band spectra. The NGC 4491 spectrum spans a narrower wavelength range than the other spectra as it has a poor S/N ratio outside of the plotted interval. As in Figure 7, there is good visual agreement between the SgrA and NGC 4491 spectra.

at visible and red wavelengths. The depths of the first overtone CO bands, NaI2.21 $\mu$ m and CaI2.26 $\mu$ m in these spectra are similar. Line indices measured from the NGC 4491 spectrum are listed in Table 3. The NGC 4491 indices tend to be smaller than those in SgrA, although the NGC 4491 NaI2.21 $\mu$ m and CO(2,0) indices still exceed those measured from the models.

A surprising result is that the emission lines in the  $K$ -band spectra of NGC 4491 and SgrA have comparable equivalent widths. These similarities are noteworthy given the marked differences between these galaxies. SgrA is at the center of a star-forming SBbc galaxy that is in a more-or-less isolated environment. The Galaxy likely has not interacted with galaxies of similar mass, although there is an entourage of dwarf companions with which there likely has been interactions. In contrast, NGC 4491 is an intermediate mass SBa(s) disk galaxy with quenched star formation in the disk; Lisker et al. (2006) classify NGC 4491 as a ‘dwarfish S0/Sa’. NGC 4491 is in a crowded environment where interactions with galaxies of similar or larger size are almost certain to have occurred.

Perhaps of greatest significance is that very different physical volumes are sampled by the SgrA and NGC 4491 spectra; NGC 4491 is three orders of magnitude more distant than the GC, and so the F2 spectrum of NGC 4491 includes light from a much larger intrinsic volume, and hence a larger number of stars, than in the SgrA F2 observations. Davidge (2018; 2020) discusses the star-forming environment of the nucleus of NGC 4491, and notes that the MIR SED of the central regions of NGC 4491 is similar to that of the starburst dwarf galaxy NGC 5253, where massive, compact clusters are forming (e.g. Calzetti et al. 2015, and references therein). Boselli et al. (2010) found that the characteristic dust temperature in its central regions is the highest of all galaxies in the Herschel Reference Survey. Even though the similarities in the NIR emission line spectra point to similar *mean* densities for the ionizing radiation field, the localized conditions in SgrA are likely not as extreme as those in NGC 4491.

## 5.2. The Spectrum of the Young Component

The SFRs compiled in Figure 14 of Pfuhl et al. (2011) indicate that while the NIR light from the center of the NSC is dominated by stars with intermediate and old ages, there is a significant contribution from stars that formed within the past  $\sim 10$  Myr. On a basic level, the spectra of any star-forming region can be thought of as the luminosity-weighted combination of light from a young stellar component and older background/foreground populations. An integrated spectrum of the young component near the GC can then be extracted by subtracting out light from the intermediate age and older components.



Models with ages of 3 and 10 Gyr and  $[\text{Fe}/\text{H}] = -0.25$  and  $+0.06$  were subtracted from the SgrA (i.e. the mean of Region 2 and 3) spectrum to assess the affect of varying age and metallicity on the resulting young spectrum. Following the Pfuhl et al. (2011) SFR summary, these models were scaled so that the older population account for  $\sim 70\%$  of the NIR light. The spectrum that results after subtracting the 3 Gyr model with  $[\text{Fe}/\text{H}] = -0.25$  is shown in Figure 9. The spectra produced by subtracting the 10 Gyr model and those with  $[\text{Fe}/\text{H}] = 0.06$  are almost identical to those shown in Figure 9.

The removal of light from old stars enhances the emission spectrum, amplifying features that are faint in the initial spectrum. As the spectra were recorded through slits then not all of the line emission is sampled. Still, the F2 slit pointings sample the strongest regions of  $\text{Br}\gamma$  and  $\text{HeI}2.06\mu\text{m}$  emission shown in Figures 7 and 8 of Feldmeier-Krause et al. (2015). The spatial distribution of the  $\text{Br}\gamma$  and  $\text{HeI}$  emission is also very similar. Hence, the SgrA emission spectrum in Figure 9 should be representative of the most vigorous star-forming areas near the center of the NSC.

$\text{Br}\gamma$  and  $\text{H}_2$  1-0 S(1) have similar strengths in the GC spectrum in Figure 9, which is consistent with what is seen in star-forming galaxies (e.g. Puxley et al. 1990). The  $\text{H}_2$  1-0 S(1) emission line in the young SgrA spectrum has a larger equivalent width than in the NGC 253 spectrum. Rosenberg et al. (2013) discuss the source of  $\text{H}_2$  emission in NGC 253. Based on the ratio of the 2-1 and 1-0 S(1)  $\text{H}_2$  lines, coupled with the similar spatial distributions of  $\text{H}_2$  and polycyclic aromatic hydrocarbon emission, they conclude that  $\text{H}_2$  emission near the center of NGC 253 likely originates from B stars.

The 2-1 S(1) line near  $2.25\mu\text{m}$  in the young GC spectrum is not clearly detected, and it is much weaker than the 1-0 line. As in NGC 253, the  $\text{H}_2$  line strengths are thus consistent with  $\text{H}_2$  emission powered by fluorescence, rather than shocks. While the comparatively large equivalent width of the 1-0 S(1) line in the young GC spectrum might suggest a higher luminosity-weighted density of lower mass ionizing stars than near the center of NGC 253, we caution that the F2 slit does not sample all parts of the star-forming region and the  $\text{H}_2$  line varies in strength from region-to-region (e.g. Yusef-Zadeh et al. 2001).

Deep absorption lines are seen in the young GC spectrum when light from bright stars is included. These deep CO bands are due in large part to IRS 7. Given that the SSP models that have been used to construct the young GC spectrum have ages well in excess of a Gyr then there could also be a contribution to the deep NIR absorption features in Figure 9 from AGB stars in populations that formed a few hundred Myr in the past. Still, it is unlikely that much the absorption features in Figure 9 originate predominantly from such a population since the SFH indicates that the SFR was low 0.5 - 1.0 Gyr in the past.

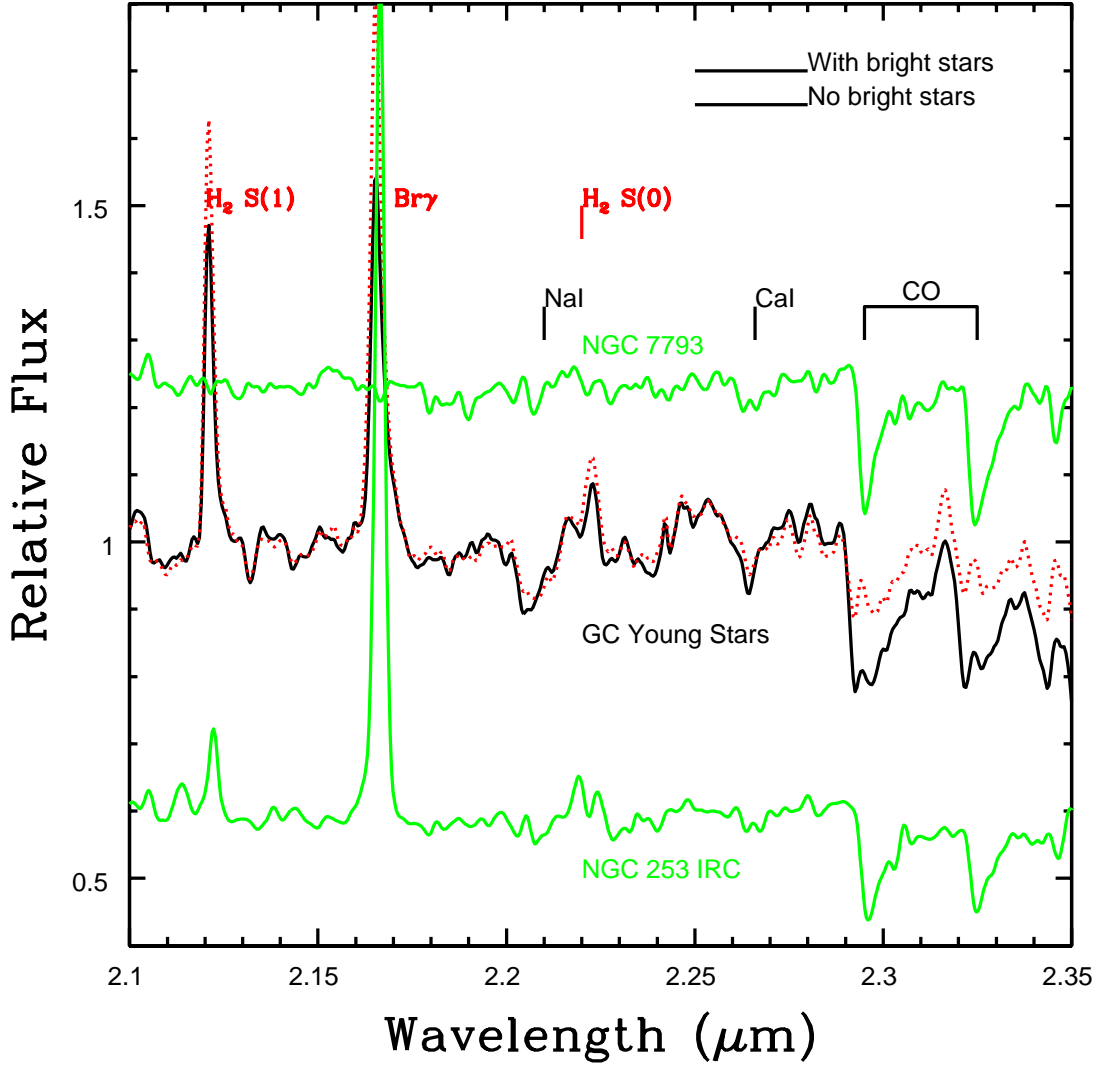


Fig. 9.— Spectrum of the young component near the GC, which was constructed by subtracting a scaled SSP spectrum with  $[\text{Fe}/\text{H}] = -0.25$  and 3 Gyr from the SgrA spectrum. The black line shows the differenced spectrum that results when light from bright stars is included, while the dashed red line shows the differenced spectrum when the light from bright stars is removed. Spectra of the center of NGC 7793 and NGC 253 from Davidge (2016) are also shown. The CO bands in the differenced spectrum provide insights into the young, cool stellar content. The deep CO bands in the black spectrum originate predominantly from IRS 7, although very luminous AGB stars that formed during the past  $\sim 1$  Gyr may also contribute to these features. The CO bands largely disappear when light from bright sources is removed, indicating that the contribution made by cool pre-main sequence objects is modest at these wavelengths.

Some types of pre-main sequence (PMS) stars might contribute to CO absorption in the integrated spectrum of a young system. Eckart et al. (2013) conclude that star formation near the GC is on-going, and Peiβker et al. (2020) identify candidate PMS stars near the center of the NSC. However, Nayakshin & Sunyaev (2005) find lower than expected X-ray emission from the inner Galaxy, suggesting low frequency of PMS stars that could be consistent with a top-heavy mass function. In fact, the mass function exponent found by Lu et al. (2013) can explain the X-ray luminosity.

FU Orionis objects are PMS stars that have a low mass and experience periodic, short-lived accretion events from a companion that causes a large increase in magnitude. These objects have deep, supergiant-like CO bands in their spectra (e.g. Hartmann et al. 2004; Connelley & Reipurth 2018), and are intrinsically much fainter than RSGs, with  $M_K \sim -1$  for the prototype star FU Orionis, making them more-or-less comparable to the brightness of red clump stars. FU Ori stars are thus within the detection limits of current photometric studies of resolved objects in the NSC, and none have been detected. Given that the outbursts that characterize FU Ori stars are also very rare, it is unlikely that they contribute significantly to the integrated NIR light. In fact, when light from bright stars is excluded then the CO bands weaken, and the significance of these features is not high given the uncertainties in the contribution that light from old and intermediate age stars make to the total population.

While NaI2.21 $\mu$ m and CaI2.26 $\mu$ m are deep in the GC young spectrum after light from bright stars is removed, these are likely an artifact of the model spectrum having NaI and CaI features that are too weak. Therefore, once light from bright stars is removed then the young spectrum can be characterized as a mainly featureless continuum, as expected given the large concentration of early-type stars that are fainter than  $K = 12$  in the inner regions of the NSC (e.g. Paumard et al. 2006; Do et al. 2013).

## 6. DISCUSSION & CONCLUSIONS

Spectra recorded with F2 on GS have been used to examine the SED of the NSC along its major axis in the wavelength interval 1.3 $\mu$ m – 2.4 $\mu$ m. The 4.3 arcmin F2 slit samples stars near the GC that formed within the past few Myr, as well as stars in the NSC, the NB, and the intermediate age/old stellar substrate of the inner regions of the Galaxy. The slit pointings cover roughly 100 arcsec<sup>2</sup> in the central parts of the NSC, while an even larger area is covered in the outer regions of the NSC.

The study of integrated light has the potential to allow the full range of stellar content in a system to be examined, including intrinsically faint objects that can not be detected

individually due to crowding and/or faintness, but that still contain important clues into the evolution of the NSC and the NB. While there are possible issues understanding the formation of lines in the NIR spectra of cool stars (e.g. Thorsbro et al. 2018), the NIR is by default the primary wavelength region for probing the stellar content of the NSC as spectra at visible wavelengths are unattainable. Studies of the integrated NIR spectrum of the NSC also enable direct comparisons with the central regions of other galaxies, allowing the nature of the inner regions of the Galaxy to be compared with those of other galaxies. For example, the detection of emission lines in the SgrA spectrum that have comparable equivalent widths to those in other galaxies would be consistent with similar characteristics in the local ionizing radiation field.

The conclusions are as follows:

1) The depths of absorption features in the integrated NIR spectrum of the NSC are *roughly* (see below) matched by that of a SSP that has a luminosity-weighted metallicity and age that is consistent with values deduced from observations of resolved stars. While this is an important check of the luminosity-weighted metallicity, it is not a tight constraint on the luminosity-weighted age, as very different SFHs can produce similar luminosity-weighted ages. Indeed, changing the assumed age by many Gyr results in only subtle differences in the spectrum of systems that are older than a few Gyr. Still, that the depths of absorption features are more-or-less reproduced indicates that (1) nebular continuum emission is likely not a major contributor to the NIR SED, as expected from the Byler et al. (2017) models if star formation was initiated more than a few Myr in the past, and (2) stochastic sampling uncertainties likely do not bias the properties of the F2 spectra.

2) The NaI2.21 $\mu$ m and CaI2.26 $\mu$ m indices vary with location in the NSC. The variations are in the sense that the equivalent widths of NaI2.21 $\mu$ m and CaI2.26 $\mu$ m near the center of the NSC are significantly larger than near the ends of the F2 slit. The same results are found after light from bright stars has been excised from the spectra, indicating that positional changes in the NaI2.21 $\mu$ m and CaI2.26 $\mu$ m indices along the slit are not restricted to the most luminous – and hence most evolved – stars near the center of the NSC.

Gallego-Cano et al. (2020) examine the spatial distribution of bright giants and red clump (RC) stars in the NSC. While lacking color information to distinguish spectral type, they argue that the RC sample is not contaminated by early-type stars, as spectroscopic surveys indicate that these tend to be clustered in the central 0.5 parsec of the NSC. Still, the identification of stars based solely on photometry in this highly extincted region can be mis-leading (e.g. Nishiyama et al. 2016).

Gallego-Cano et al. (2020) find that the ratio of bright giants to RC stars varies with distance from the center of the NSC outside of the central 0.5 parsecs, where there has been recent star formation, and they interpret this as a consequence of incomplete mixing of populations that have different ages – i.e. there is an age gradient. Such a gradient might be expected if the central regions of the NSC have been the site of previous star-forming episodes over an extended period of time given the finite time required for stars to diffuse away from the center of the NSC. That the NaI2.21 $\mu$ m and CaI2.26 $\mu$ m indices in Regions 1 and 4 differ from those in Regions 2 and 3 is consistent with a gradient in the properties of cool stars in the NSC. While we lack adequate spectroscopic diagnostics to attribute convincingly the gradients in these indices to age, the indices measured from the model spectra decrease in strength with increasing age, which is *qualitatively* consistent with the sense of the expected age gradient suggested by Gallego-Cano et al. (2020). However, a gradient solely in age can not explain the very large NaI2.21 $\mu$ m and CaI2.26 $\mu$ m indices found in Regions 2 and 3.

The NaI2.21 $\mu$ m and CaI2.26 $\mu$ m indices in Regions 1 and 4 match those predicted by models that have solar abundance mixtures, whereas near the center of the NSC they are deeper than predicted by the same models. The NaI2.21 $\mu$ m and CaI2.26 $\mu$ m indices are not sensitive to uncertainties in plausible age and metallicity estimates. Moreover, the deeper than expected NaI and CaI indices are found after light from the brightest stars is removed. This argues that Na and Ca abundances near the center of the NSC are larger than expected for a solar chemical mixture over a range of stellar evolutionary states, and not just among the luminous stars where deeper than expected Na I and Ca I features were first reported by Sellgren et al. (1987) and Blum et al. (1996). More recently, Feldmeier-Krause et al. (2017b) also find NaI lines in the spectra of stars in the NSC that are deeper than in stellar libraries, which presumably reflect solar metallicities and chemical mixtures.

The depths of Na I lines are sensitive to surface gravity, and during the past decade various Na features have been used to examine the mass function in integrated light. NaI2.21 $\mu$ m is not as sensitive to the mass function as other Na lines at visible/NIR wavelengths, but is an effective probe of [Na/Fe] (Alton et al. 2018). The deep NaI2.21 $\mu$ m indices in Regions 2 and 3 might then suggest that the majority of stars in the central regions of the NSC formed from material that originated in an environment that produced super-solar abundances of either Na and/or of elements and molecules with transitions that are also sampled by the NaI2.21 $\mu$ m index, such as Sc, V, and CN (Carr et al. 2000). A non-solar chemical mixture has been proposed for stars near the center of the NSC by Do et al. (2018), although those results have been challenged by Thorsbro et al. (2018).

Non-solar Na mixtures are not typical of chemical enrichment in a quiescent environment like a thin disk. Rather, a Na over-abundance could result in material that experi-

enced rapid enrichment by very massive stars (e.g. Kobayashi et al. 2006) with suppressed subsequent enrichment from lower mass stars. A top-heavy IMF will also result in an overabundance of Na. Such abundances are reminiscent of those in globular clusters, for which exotic chemical enrichment paths have been proposed (e.g. Denissenkov & Hartwick 2014; Gieles et al. 2018). Massive spheroids show steep gradients in  $[\text{Na}/\text{Fe}]$  (Alton et al. 2018; Sarzi et al. 2018), suggesting that the Na yield changes with radius in these systems. The behaviour of  $\text{NaI}2.21\mu\text{m}$  at locations along the F2 slit is reminiscent of that seen in vastly larger systems, albeit on a much smaller scale.

In contrast to the central regions of the NSC, the  $\text{NaI}2.21\mu\text{m}$  and  $\text{CaI}2.26\mu\text{m}$  indices in Regions 1 and 4, where the fractional contribution by light from NB and older bulge stars is much higher than near the center of the NSC, have equivalent widths that are consistent with a scaled-solar chemical mixture. Lee et al. (2018) examine the spectra of red clump stars at high latitudes in the Galactic bulge, and find similarities with the spectroscopic properties of their counterparts in globular clusters. However, the stars observed by Lee et al. (2018) are not in the NB. Some models of bulge formation predict radial gradients in stellar content, with stars in the NSC and close to the disk plane forming from disk material (e.g. Buck et al. 2018).

3) The NIR emission line characteristics of the NSC are consistent with it being a ‘typical’ nucleus in terms of the fractional amount of NIR light that comes from recently formed stars. This further reinforces the notion that the stellar content of the Galactic NSC is broadly similar to nuclear clusters in other galaxies (e.g. Neumayer et al. 2020). When light from the old bulge, the NB, the NSC, and the youngest stars are included, the integrated spectrum of the NSC shows (fortuitously!) good agreement with the emission and absorption components of the spectrum of the early-type Virgo cluster disk galaxy NGC 4491. The agreement between the equivalent widths of emission lines does not indicate similar total SFRs. Rather, given the vastly different distances of the GC and NGC 4491 then it indicates similar densities of ionizing stars and older stars in the volumes sampled by each spectrum. The specific SFRs in the areas sampled are thus likely similar.

The similarity in the depths of the absorption components of the SgrA and NGC 4491 spectra reflects the comparable luminosity-weighted ages and metallicities of the areas sampled in NGC 4491 and by the F2 slit near the GC. Of particular note is that the  $\text{NaI}2.21\mu\text{m}$  and  $\text{CaI}2.26\mu\text{m}$  features in the NGC 4491 and SgrA spectra have very similar depths, whereas they are much shallower in the NGC 7793 and NGC 253 spectra. This does not mean that the comparatively deep  $\text{NaI}2.21\mu\text{m}$  and  $\text{CaI}2.26\mu\text{m}$  features in the NSC spectrum are absent near the centers of those galaxies, as angular resolution limitations may prevent the detection of super-solar NaI and CaI features if they are restricted to the compact central regions

which may not yet have been resolved. Indeed, the area over which super-solar  $\text{NaI}2.21\mu\text{m}$  and  $\text{CaI}2.26\mu\text{m}$  absorption is found is very different in NGC 4491 and the MW, occurring over a much larger area in the Virgo cluster galaxy than in the central regions of the NSC.

4) An integrated spectrum of the young population in the central regions of the NSC has been extracted by subtracting a SSP model spectrum that serves as a proxy for the intermediate age and old stars along the NSC sight line. The results are not sensitive to the age and metallicity of the model that is subtracted from the spectrum. The spectrum of the young component that results when light from bright stars is removed is largely continuum-dominated, while the spectrum constructed with light from bright stars intact shows prominent absorption features that are attributed to evolved red stars.

The equivalent widths of many of the emission lines are similar to those in the central regions of NGC 253. This does not indicate that the innermost regions of the Galaxy is experiencing a wide-scale starburst like that in NGC 253, as NGC 253 is much more distant than the GC, and so a larger volume is sampled in that galaxy (Section 5). Rather, the similarity in equivalent widths indicates that the densities of ionizing sources in the volumes sampled are similar. Such agreement was foreshadowed by the similarity between excitation conditions in the inner Galaxy and M82 noted by Simpson et al. (1999), who described the GC as an aging star burst. It has been suggested that the SFR near the GC is low, possibly due to the internal gas kinematics of molecular clouds in this area (e.g. Kauffmann et al. 2017). However, the comparison with NGC 253 suggests that this is not the case near the center of the NSC.

That the integrated NIR spectrum of the youngest stars near the GC is similar to that of NGC 253 is indirect evidence that the young stars detected in the central parsec did not form during a single event, but that star formation has occurred more-or-less continuously for many Myr near the center of the NSC. The basis for this claim is that – barring a fluke coincidence in SFHs – the similarity between the equivalent widths of emission lines in NGC 253 and the GC can plausibly be attributed to the convergence of spectroscopic properties in systems that form stars in a continuous (or near-continuous) manner, as predicted by models of spectrophotometric evolution (e.g. Byler et al. 2017). Barnes et al. (2017) conclude that the SFR in the inner regions of the Galaxy has been more-or-less continuous during the past few Myr. We note that the star-forming activity near the GC need not be strictly continuous to produce convergence in emission line properties, and could result if individual star formation episodes are separated on Myr timescales (i.e. a large fraction of the evolutionary timescales of very massive stars), thereby producing gaps in activity that could still maintain a steady supply of ionizing radiation.

An age dispersion among young stars near the center of the NSC would suggest that if star formation has occurred more-or-less continuously *in situ* then either star-forming material can survive for many Myr in the GC environment or that there is a steady supply of molecular clouds to replace those that are destroyed by tidal forces related to SgrA\* (e.g. discussion by Tsuboi et al. 2016). The distribution of OB stars (e.g. Feldmeier-Krause et al. 2015) supports the notion of *in situ* star formation near the center of the NSC. The very recent SFH of the central regions of the NSC may then not be too different from that in massive young clusters in the Galactic disk, despite the obvious differences in environment. Evidence for star formation that extends over a few Myr has been found in young massive Galactic clusters, such as Westerlund 1 (e.g. Lim et al. 2013), while the age range in larger star-forming complexes may exceed 10 Myr (e.g. de Marchi et al. 2011). There is also evidence that star formation in clusters may not be continuous, but might be distributed over a few episodes (e.g. Beccari et al. 2017).

There are obvious avenues for future work. Each of the four regions considered in this paper sample  $\sim 50 - 65 \text{ arcsec}^2$  along the major axis of the NSC, and there is an obvious motivation to obtain integrated light spectra over a larger angular area at large angular offsets from the center of the NSC, with particular emphasis on the interval 2 – 4 parsecs along the NSC major axis, where star counts indicate that the stellar content is changing (Gallego-Cano et al. 2020). The heavy extinction at Galactic latitudes south of the GP restricts such work to the area north of the GP. IFUs are an obvious tool for expanding sky coverage, although there are potential issues with sky subtraction, as a suitably large area of high obscuration must be observed to monitor the background in an absolute sense. This may bias studies with the best sky subtraction to those that sample small fields of view. A merit of long slit spectroscopy is that the areas of high obscuration that are close to the GC define extended filaments that run more-or-less parallel to the GP, making it possible to monitor background light close to the center of the NSC.

Background light considerations mean that not all existing IFU spectroscopic GC datasets may be suitable for the study of integrated light. Some have been recorded with the goal of examining only individual sources, for which only a local sky background must be known (e.g. Do et al. 2013). There are possible exceptions: Eckart et al. (2013), Feldmeier-Krause et al. (2015), and Peißker et al. (2020) monitored background light by observing a dark cloud  $\sim 14 \text{ arcmin}$  from the GC. However, in the case of the KMOS spectra obtained by Feldmeier-Krause et al. (2015) only one quarter of the IFUs sampled the dark cloud, and so it is not clear if the background is known well enough across the mosaiced area to obtain reliable integrated light spectra. A limitation of the extant IFU spectroscopic surveys is that they cover only the central parsec of the NSC, and so do not sample the NSC out to the radii covered by the F2 spectra.



Observations with a higher wavelength resolution would also be of interest to determine if the NaI2.21 $\mu$ m and CaI2.26 $\mu$ m features track contributions from Na and Ca, or are skewed by other elements as suggested by Carr et al. (2000) in their study of IRS 7. A consideration is that the velocity dispersion of the stars in the area studied define inherent limits on the wavelength resolution of integrated light spectra. The limiting wavelength resolution of integrated light spectra throughout much of the area sampled by F2 is  $\frac{\lambda}{\Delta\lambda} \sim 5000 - 10000$ . The observations shown in Figure 6 of Carr et al. (2000) suggest that such a spectroscopic resolution should be sufficient to resolve lines of Sc and V that are close to the 2.21 $\mu$ m NaI lines. There is a rise in the intrinsic velocity dispersion near SgrA\*, with  $\sigma \sim 160$  km/sec at 1 arcsec radius (Trippe et al. 2008). The peak in velocity dispersion in the central arcsec sets the limiting spectral resolution to a few thousand, complicating efforts to resolve these lines in integrated light.

Spectroscopic observations with a higher angular resolution will also be of obvious interest for probing the central arcsec around SgrA\*, as this is where the stellar density effects are most extreme, and the impact of the severe environment near SgrA\* most pronounced. One result may be the formation of objects that are unique to this environment (e.g. Ciurlo et al. 2020). There is a dearth of bright late-type stars in the central arcsec (e.g. Do et al. 2009), while the spectra of the GC in the 2 – 2.4 $\mu$ m wavelength region discussed by Figer et al. (2000) show that the light within an arcsec of SgrA\* is dominated by young stars. Most of the early-type stars in this area have spectral-type B (Eisenhauer et al. 2005) and are on the main sequence (Habibi et al. 2017).

We close by noting that high angular resolution observations of integrated light may also allow the mass function among low mass stars near SgrA\* to be probed with the NaI2.21 $\mu$ m doublet, although there is degeneracy with [Na/Fe]. While the number density, spatial distribution, and mass function of sub-solar mass main sequence stars have yet to be explored in the central arcsec, it is intriguing that the 2.21 $\mu$ m NaI feature in the Figer et al. (2000) spectra diminishes in strength with decreasing projected distance from SgrA\*, although the spectra in this area will have to be modelled with an appropriate mix of stellar content. While observations of other Na transitions may lift the degeneracy with [Na/Fe], observing Na transitions shortward of  $\sim 1.3\mu$ m in the NSC is problematic due to the high line-of-sight extinction. The NaI doublet near 2.34 $\mu$ m may provide useful supplementary information to interpret the NaI2.21 $\mu$ m results, as this feature is prominent in late M dwarfs (e.g. Rayner et al. 2009). A complicating factor is that this feature is located close to the  $^{13}\text{CO}$  2–0 band head at 2.345 $\mu$ m, compromising detection in spectra with low wavelength resolution. This feature is not detected convincingly in the F2 spectra, but may be present in the spectra discussed by Feldmeier et al. (2014) in their Figure 3.

It is a pleasure to thank the anonymous referee for providing a prompt, comprehensive, and helpful review that greatly improved the paper.

## REFERENCES

- Alexander, T. 1999, *ApJ*, 527, 835
- Alexander, T. 2005, *PhR*, 419, 65
- Alton, P. D., Smith, R. J., & Lucey, J. R. 2018, *MNRAS*, 478, 4464
- Amaro-Seoane, P., & Chen X. 2014, *ApJ*, 781, L18
- Antonini, F., Cappuzzo-Dolcetti, R., Mastrobuono-Battisti, A., & Merritt, D. 2012, *ApJ*, 750, 111
- Arca-Sedda, M. & Cappuzzo-Dolcetti, R. 2014, *MNRAS*, 444, 3738
- Barnes, A. T., Longmore, S. N., Battersby, C., Bally, J., Kruijssen, J. M. D., Henshaw, J. D., & Walker, D. L. 2017, *MNRAS*, 469, 2263
- Bartko, H., Martins, F., Fritz, T. K., et al. 2009, *ApJ*, 697, 1741
- Bartko, H., Martins, F., Trippe, S., et al. 2010, *ApJ*, 708, 834
- Becarri, G., Petr-Gotzens, M. G., Boffin, H. M. J., et al. 2017, *A&A*, 604, A22
- Bensby, T., Feltzing, S., Gould, A., et al. 2017, *A&A*, 605, A89
- Blum, R. D., Sellgren, K., & Depoy, D. L. 1996, *AJ*, 112, 1988
- Boselli, A., Eales, S., Cortese, L. et al. 2010, *PASP*, 122, 261
- Buchholz, R. M., Schödel, R., & Eckart, A. 2009, *A&A*, 499, 483
- Buck, T., Ness, M. K., Maccio, A. V., Obreja, A., & Dutton, A. A. 2018, *ApJ*, 861, 88
- Byler, N., Dalcanton, J. J., Conroy, C., & Johnson, B. D. 2017, *ApJ*, 840, 44
- Calzetti, D., Johnson, K. E., Adamo, A. et al. 2015, *ApJ*, 811, 75
- Carr, J. S., Sellgren, K., & Balachandran, S. C. 2000, *ApJ*, 530, 307
- Chabrier, G. 2001, *ApJ*, 554, 1274
- Ciurlo, A., Paumard, T., Rouan, D., & Clénet, Y. 2016, *A&A*, 594, A113
- Ciurlo, A., Campbell, R. D., Morris, M. R., et al. 2020, *Nature*, 577, 337
- Connelley, M. S., & Reipurth, B. 2018, *ApJ*, 861, 145
- Conroy, C., & van Dokkum, P. 2012, *ApJ*, 747, 69

- Cordier, D., Pietrinferni, A., Cassisi, S., & Salaris, M. 2007, *AJ*, 133, 468
- Cunha, K., Smith, V. V., Johnson, J. A., et al. 2015, *ApJ*, 798, L41
- Dahmer-Hahn, L. G., Riffel, R., Rodriguez-Ardila, A. et al. 2018, *MNRAS*, 476, 4459
- Dale, J. E., Davies, M. B., Church, R. P., & Freitag, M. 2009, *MNRAS*, 393, 1016
- Davidge, T. J. 1998, *AJ*, 115, 2374
- Davidge, T. J. 2016, *ApJ*, 818, 142
- Davidge, T. J. 2018, *AJ*, 156, 233
- Davidge, T. J. 2020, *AJ*, 159, 186
- Davidge, T. J., Simons, D. A., Rigaut, F., Doyon, R., & Crampton, D. 1997, *AJ*, 114, 2586
- de Marchi, G., Paresce, F., Panagia, N., et al. 2011, *ApJ*, 739, 27
- Denissenkov, P. A., & Hartwick, F. D. A. 2014, *MNRAS*, 437, L21
- Do, T., Ghez, A. M., Morris, M. R., Lu, J. R., Matthews, K., Yelda, S., & Larkin, J. 2009, *ApJ*, 703, 1323
- Do, T., Lu, J. R., Ghez, A. M., Morris, M. R., Yelda, S., Martinez, G. D., Wright, S. A., & Matthews, K. 2013, *ApJ*, 764, 154
- Do, T., Kerzendorf, W., Konopacky, Q., Marcinik, J. M., Ghez, A., Lu, J. R., & Morris, M. R. 2018, *ApJ*, 855, L5
- Do, T., Hees, A., Ghez, A., et al. 2019, *Science*, 365, 664
- Eckart, A., & Genzel, R. 1997, *MNRAS*, 284, 576
- Eckart, A., Muzic, K., Yazici, S., et al. 2013, *A&A*, 551, A18
- Eikenberry, S., Elston, R., Raines, S. N. et al. 2004, *Proc. SPIEE*, 5492, 1196
- Eisenhaur, F., Genzel, R., Alexander, T. et al. 2005, *ApJ*, 628, 246
- Ekers, R. D., van Gorkum, J. H., Schwarz, H. J., & Gosds, W. M. 1983, *A&A*, 122, 143
- Feldmeier, A., Neumayer, N., Seth, A., et al. 2014, *A&A*, 570, A2
- Feldmeier-Krause, A., Neumayer, N., Schödel, R., et al. 2015, *A&A*, 584, A2
- Feldmeier-Krause, A., Zhu, L., Neumayer, N., van de Ven, G., de Zeeuw, P. T., & Schödel 2017a, *MNRAS*, 466, 4040
- Feldmeier-Krause, A., Kerzendorf, W., Neumayer, N., et al. 2017b, *MNRAS*, 464, 194
- Ferraro, F. R., Montegriffo, P., Origlia, L., & Fusi Pecci, F. 2000, *AJ*, 119, 1282
- Figer, D. F., Becklin, E. E., McLean, I. S., et al. 2000, *ApJ*, 533, L49

- Frogel, J. A., Stephens, A., Ramirez, S., & DePoy, D. L. 2001, *AJ*, 122, 1896
- Gallego-Cano, E., Schödel, E., Dong, H., Nogueras-Lara, F., Gallego-Calvente, A. J., Amaro-Seoane, P., & Baumgardt, H. 2018, *A&A*, 609, A26
- Gallego-Cano, E., Schödel, R., Nogueras-Lara, F., et al. 2020, *A&A*, 634, A71
- Genzel, R., Schödel, R., Ott, T. et al. 2003, *ApJ*, 594, 812
- Genzel, R., Eisenhauer, F., & Gillessen, S. 2010, *RvMP*, 82, 3121
- Ghez, A. M., Klein, B. L., Morris, M., & Becklin, E. E. 1998, *ApJ*, 509, 678
- Ghez, A., Duchêne, G., Matthews, K., et al. 2003, *ApJ*, 586, L127
- Gieles, M., Charbonnel, C., Krause, M. G. H., et al. 2018, *MNRAS*, 478, 2461
- Gillessen, F., Eisenhauer, F., Fritz, T. K. et al. 2009, *ApJ*, 707, L114
- Gonneau, A., Lyubenova, M., Lancon, A. et al. 2020, *A&A*, 634, A133
- Gratton, R. G., Carretti, E., & Bragaglia, A. 2012, *A&ARv*, 20, 50
- Habibi, M., Gillessen, S., Martins, F., et al. 2017, *ApJ*, 847, 120
- Hartmann, L., Hinkle, K., & Calvet, N. 2004, *ApJ*, 609, 906
- Haubois, X., Perrin, G., Lacour, S., et al. 2009, *A&A*, 508, 923
- Kacharov, N., Neumayer, N., Seth, A. C., Cappellari, M., McDermid, R., Walcher, C. J., & Böker, T. 2018, *MNRAS*, 480, 1973
- Kauffmann, J., Pillai, T., Zhang, Q., et al. 2017, *A&A*, 603, A90
- Kobayashi, C., Umeda, H., Nomoto, K., Tominaga, N., & Ohkubo, T. 2006, *ApJ*, 653, 1145
- Krabbe, A., Genzel, R., Eckart, A., et al. 1995, *ApJ*, 447, L95
- Launhardt, R., Zylka, R., & Mezger, P. G. 2002, *A&A*, 384, 112
- Lee, Y-W., Hong, S., Lim, D., Chung, C., Jang, S., Kim, J. J., & Joo, S-J 2018, *ApJ*, 862, L8
- Lim, B., Chun, M-Y, Sung, H., et al. 2013, *AJ*, 145, 46
- Lisker, T., Grebel, E. K., & Binggeli, B. 2006, *AJ*, 132, 497
- Lu, J. R., Do, T., Ghez, A. M., Morris, M. R., Yelda, S., & Matthews, K. 2013, *ApJ*, 764, 155
- Maraston, C. 2005, *MNRAS*, 362, 799
- Morris, M. 1993, *ApJ*, 408, 496
- Nandakumar, G., Ryde, N., Schultheis, M. et al. 2018, *MNRAS*, 478, 4374

- Nayakshin, S., & Sunyaev, R. 2005, MNRAS, 364, L23
- Neumayer, N., Seth, A., & Böker, T. 2020, ARA&A, 28, 4
- Nishiyama, S., Schödel, R., Yoshikawa, T., Nagata, T., Minowa, Y., & Tamura, M. 2016, A&A, 588, A49
- Nogueras-Lara, F., Schödel, R., Dong, H. et al. 2018a, A&A, 620, A83
- Nogueras-Lara, F., Gallego-Calvente, A. T., Dong, H., et al. 2018b, A&A, 610, A83
- Paumard, T., Maillard, J-P, & Morris, M. 2004, A&A, 426, 81
- Paumard, T., Genzel, R., Martins, F. et al. 2006, ApJ, 643, 1011
- Paumard, T., Pfuhl, O., Martins, F., et al. 2014, A&A, 568, A85
- Peißker, F., Hosseini, S. E., Zajacek, M. et al. 2020, A&A, 634, A35
- Pfuhl, O., Fritz, T. K., Zilka, M. et al. 2011, ApJ, 741, 108
- Pietrinferni, A., Cassisi, S., Salaris, M., & Castelli, F. 2004, ApJ, 612, 168
- Puxley, P. J., Hawarden, T. G., & Mountain, C. M. 1990, ApJ, 364, 77
- Rayner, J. T., Cushing, M. C., & Vacca, W. D. 2009, ApJS, 185, 289
- Renzini, A., Gennaro, M., Zoccali, M., et al. 2018, ApJ, 863, 16
- Rich, R. M., Ryde, N., Thorsbro, B., Fritz, T. K., Schultheis, M., Origlia, L., & Jönsson, H. 2017, AJ, 154, 239
- Rock, B., Vazdekis, A., Ricciardelli, E. et al. 2016, A&A, 589, 73
- Rock, B., Vazdekis, A., La Barbera, F., Peletier, R. F., Knapen, J. H., Allende-Prieto, C., & Aguado, D. S. 2017, MNRAS, 472, 361
- Rosenberg, M. J. F., van der Werf, P. P., & Isreal, F. P. 2013, A&A, 550, A12
- Sarzi, M., Spiniello, C., La Barbera, F., Krajnovic, D., & van den Bosch, R. 2018, MNRAS, 478, 4084
- Schödel, R., Najarro, F., Muzic, K., & Eckart, A. 2010, A&A, 511, A18
- Schödel, R., Feldmeier, A., Kunneriath, D., Stolovy, S., Neumayer, N., Amaro-Seoane, P., & Nishiyama, S. 2014, A&A, 566, A47
- Schödel, R., Gallego-Cano, E., Dong, H., Nugueras-Lara, F., Gallego-Calvente, A. T., Amaro-Seoane, P., & Baumgardt, H. 2018, A&A, 609, A27
- Schultheis, M., Rich, R. M., Origlia, L., Ryde, N., Nandakumar, G., Thorsbro, B., & Neumayer, N. 2019, A&A, 627, A152
- Sellgren, K., Hall, D. N. B., Kleinmann, S. G., & Scoville, N. 1987, ApJ, 317, 881

- Seth, A., Agueros, M., Lee, D., & Basu-Zych, A. 2008, *ApJ*, 678, 116
- Shields, J. C., Rix, H-W, Sarzi, M. et al. 2007, *AJ*, 115, 2374
- Simpson, J. P., Willeborn, F. C., Cohen, M., & Price, S. D. 1999, *The Central Parsec of the Galaxy*, ASP Conference, 186 (H. Falcke, A. Cotera, W. J. Duschl, F. Melia, & M. J. Rieke eds).
- Skidmore, W., Dell’Antonio, I., Fukugawa, M. et al. 2015, *Thirty Meter Telescope Detailed Science Case: 2015*, arXiv:1505.01195
- Stanway, E. R., & Eldridge, J. J. 2018, *MNRAS*, 479, 75
- Terndrup, D. M., Frogel, J. A., & Whitford, A. E. 1991, *ApJ*, 378, 742
- Thorsbro, B., Ryde, N., Schultheis, M., et al. 2018, *ApJ*, 866, 52
- Trippe, S., Gillessen, S., Gerhard, O. E. et al. 2008, *A&A*, 492, 419
- Tsuboi, M., Kitamura, Y., Miyoshi, M., Uehara, K., Tsutsumi, T., & Miyazaki, A. 2016, *PASJ*, 68, L7
- Villaume, A., Conroy, C., Johnson, B., Rayner, J., Mann, A. W., & van Dokkum, P. 2017, *ApJS*, 230, 23
- Yusef-Zadeh, F., Stolovy, S. R., Burton, M., Wardle, M., & Ashley, M. C. B. 2001, *ApJ*, 560, 749
- Yusef-Zadeh, F., Bushouse, H., & Wardie, M. 2012, *ApJ*, 744, 24